Contents

INSTITUTO DE PLASMAS E FUSÃO NUCLEAR

Aerodynamic Analysis of a Scramjet Inlet and Isolator

Inês Micaela da Costa Cardoso

Supervisor:
Prof. Mário António Prazeres Lino da Silva

Examination Committee:
Chairperson: Prof. Filipe Szolnoky Ramos Pinto Cunha
Supervisor: Prof. Mário António Prazeres Lino da Silva
Member of the Committee: Prof. José Carlos Fernandes Pereira

January 2021

Contents

Fig 1. Scramjet Concept Art **[1]**.

Contents

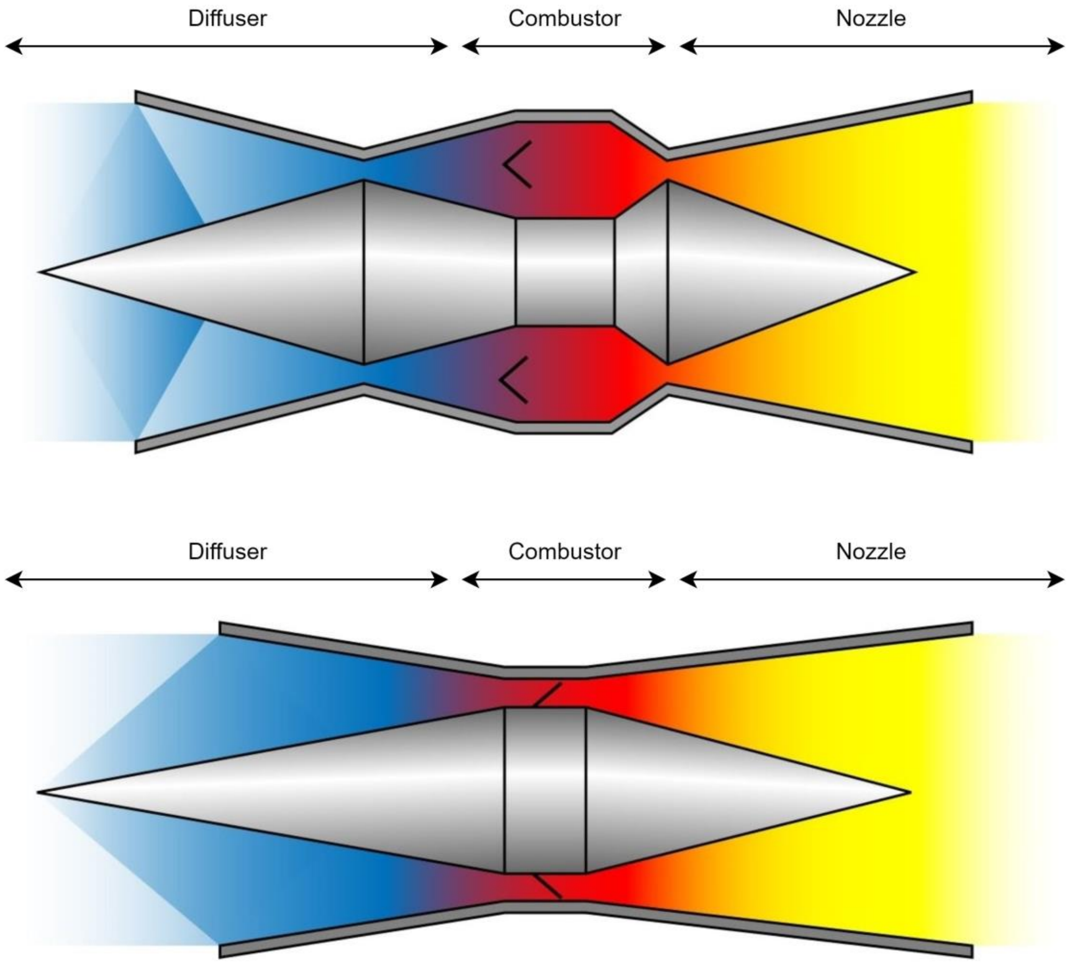

Fig. 2: Ramjet (top) and Scramjet (bottom) schematics. Adapted from **[2]**.

Ramjet

Diffuser
Air is compressed to **subsonic** speeds by means of a shock wave system.

↓

Combustor
Fuel is mixed with the compressed air and **subsonic** combustion takes place.

↓

Nozzle
The high temperature exhaust is accelerated.

↓

Thrust is generated.

Contents

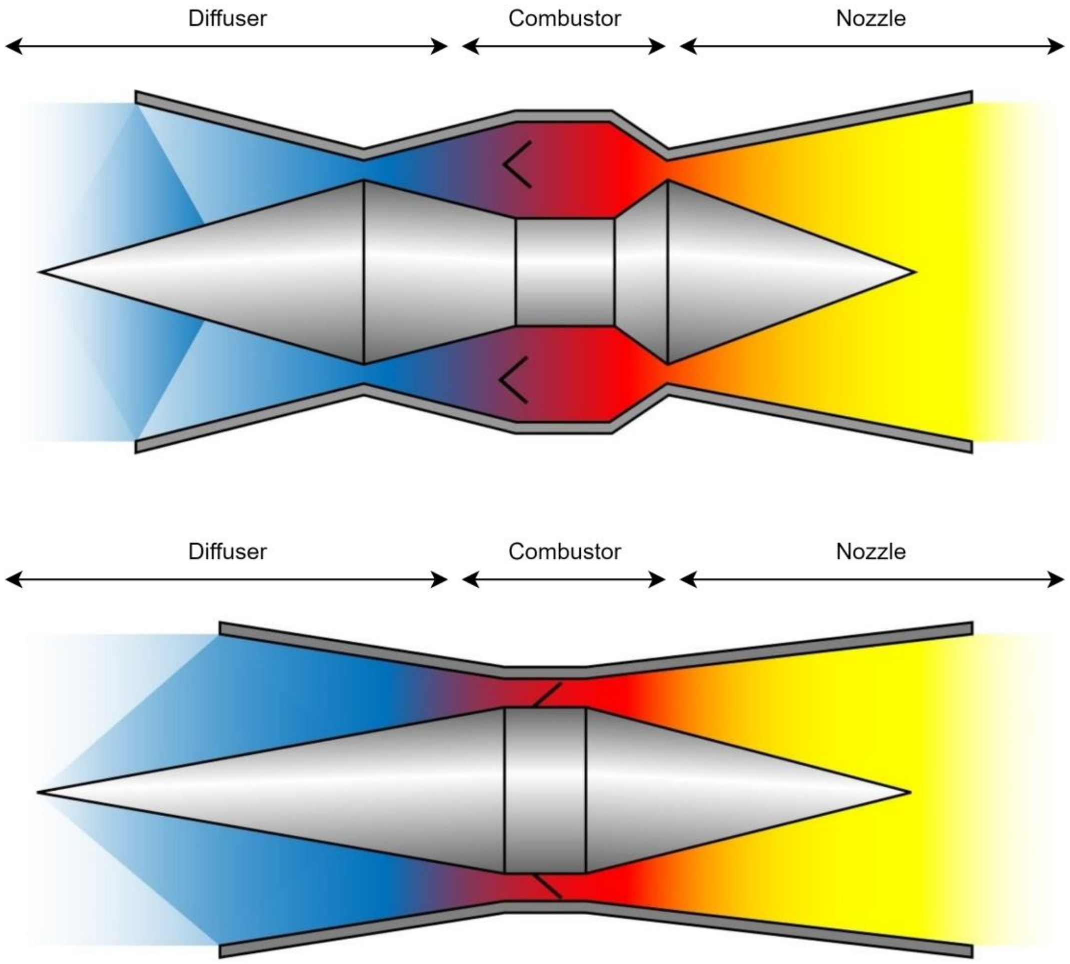

Fig. 2: Ramjet (top) and Scramjet (bottom) schematics. Adapted from **[2]**.

Scramjet

Diffuser

Air is compressed to **supersonic** speeds by means of a shock wave system.

↓

Combustor

Fuel is mixed with the compressed air and **supersonic** combustion takes place.

↓

Nozzle

The high temperature exhaust is accelerated.

↓

Thrust is generated.

Operating Conditions

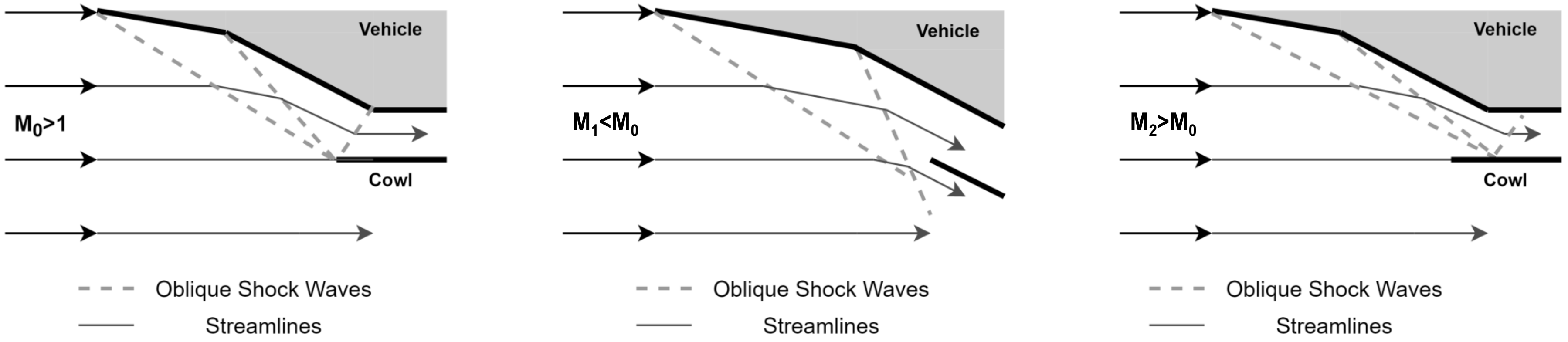

Fig. 3: *Shock-on-lip* condition (left), flow spillage (centre) and flow instability (right). Adapted from **[3]**.

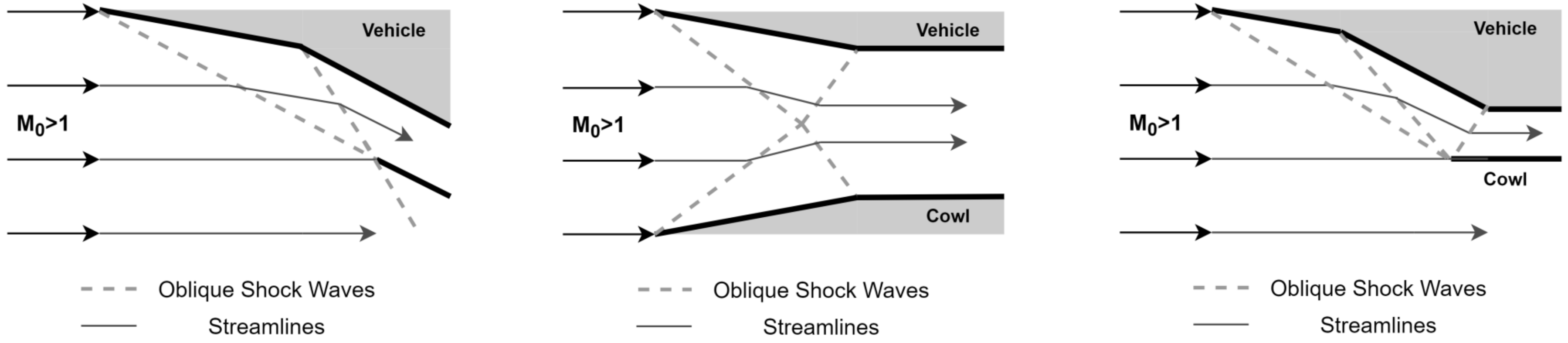

Fig. 4: External (left), internal (centre) and mixed (right) compression system layouts. Adapted from **[3]**.

Contents

ipfn
INSTITUTO DE PLASMAS E FUSÃO NUCLEAR

Objectives

- Identification of a trajectory point of interest;
- Pre-analysis of a case study from the literature;
  - Validation of the SPARK code for solving scramjet compression system flows;
  - Identification of model shortfalls and their impact on the obtained flow.
- Assess the relative importance of non-equilibrium and high temperature effects;
- Compare the performance of the two-dimensional inlet present in the case study with that of an axisymmetric inlet with the same area and pressure ratios;
- Geometry parametric study;
  - Numerically assess the influence of several geometric parameters on the behaviour of the flow within the compression system.
- Study of an off-design trajectory point;
  - Numerically assess how performance is affected at an off-design trajectory point of Mach 7.

Contents

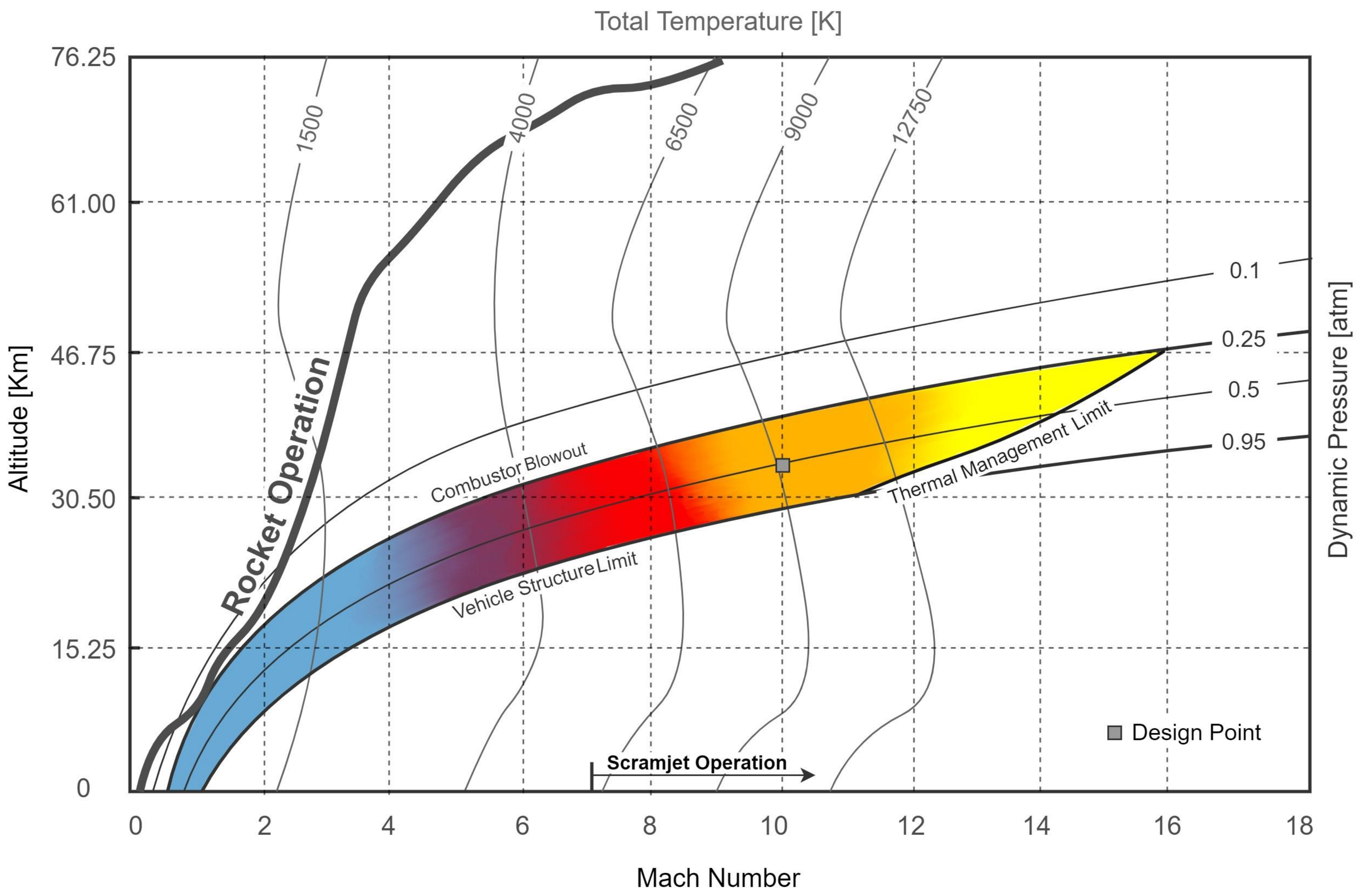

Fig. 5: Flight corridor as a function of Mach number and altitude. Identification of the selected trajectory point. Adapted from **[4]**.

Contents

Design Considerations

- The isolator should be long enough to prevent inlet unstart. The chosen reference presented an isolator length, **L = 0.5m.**
- The same reference suggests that, for a combustor entry velocity of 2400m/s and temperatures above 1000K, a back pressure of **50kPa** is expected to prevent inlet unstart and an acceptable combustor length.
- However supersonic combustion is expected to occur for isolator exit pressures as low as **20kPa [6].**

$\theta_1 [^\circ]$	$\theta_2 [^\circ]$	H [m]	H/h
6.5	8.4	0.250	10

Table 1: Design Parameters for the baseline two-dimensional inlet **[5]**.

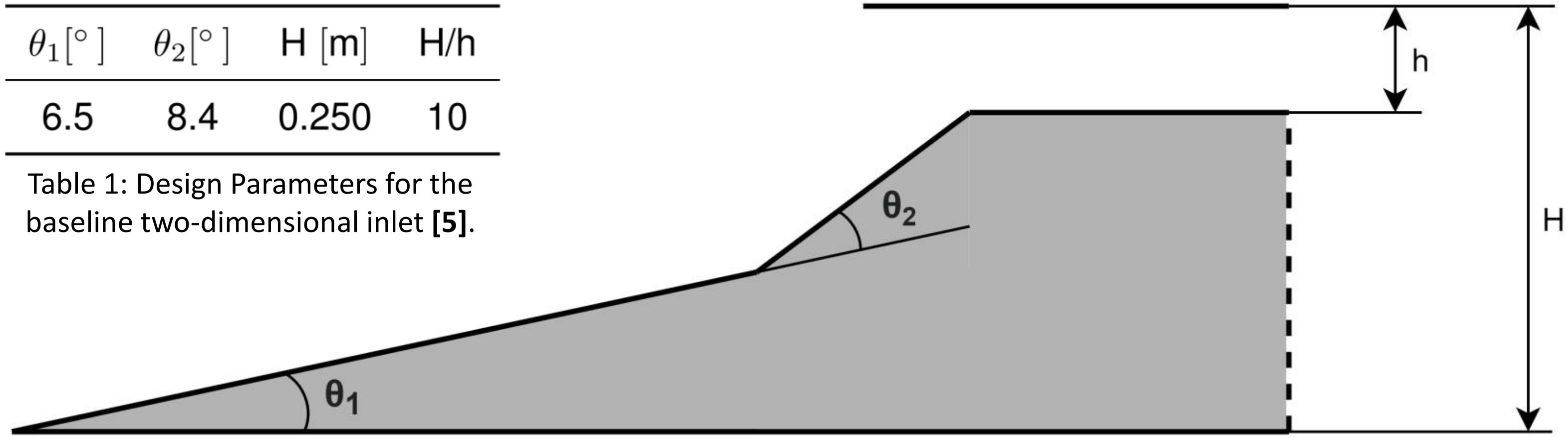

Fig. 6: Schematics of a mixed compression system. Design based on oblique shock theory.

Contents

IST
ipfn INSTITUTO DE PLASMAS E FUSÃO NUCLEAR

Non-Equilibrium Chemically Reacting Flow

- Navier-Stokes conservation equations apply, under the assumption of a continuum medium.
- The gas was considered to be a mixture of several chemical species to account for chemical reactions;
  - Considered species include: N_2, N, O_2, O, NO. No ionized species were considered.
- Thermal non-equilibrium is also expected to occur as a consequence of high temperature effects.
  - A two-temperature model, which considers the translational mode to be in equilibrium with the rotational mode, and the vibrational mode to be in equilibrium with the electronic mode was selected.

Oblique Shock Wave Theory

- Owing to its simplicity, oblique shock wave theory was used to dimension the different considered compression systems;
  - The Taylor Maccoll analysis was employed in the design of an axisymmetric compression system.

IST ipfn INSTITUTO DE PLASMAS E FUSÃO NUCLEAR

Compression System Performance

- **Total pressure ratio** between isolator exit and freestream conditions;

$$\pi_c = \frac{p_{t_c}}{p_{t_\infty}} = \frac{p_c}{p_\infty}\left\{\frac{1+\frac{\gamma-1}{2}\mathrm{Ma}_c^2}{1+\frac{\gamma-1}{2}\mathrm{Ma}_\infty^2}\right\}^{\frac{\gamma}{\gamma-1}}$$

- **Kinetic energy efficiency**, the ratio between the square of the velocity that the flow at the compression system exit would achieve if it were isentropically expanded to the freestream static pressure and the square of the freestream velocity;

$$\eta_{\mathrm{KE}} = 1 - \frac{2}{(\gamma-1)\mathrm{Ma}_\infty^2}\left\{\frac{T_c}{T_\infty}\left(\frac{p_c}{p_\infty}\right)^{-\frac{\gamma-1}{\gamma}} - 1\right\}$$

- **Compression efficiency**, the ratio of change in enthalpy that the flow at the combustor entry (or isolator exit) would incur if it were isentropically expanded to freestream static pressure, divided by the change in enthalpy that the flow is effectively put through.

$$\eta_c = \frac{(T_c/T_\infty) - (T_c/T_\infty)(p_c/p_\infty)^{-\frac{\gamma-1}{\gamma}}}{(T_c/T_\infty) - 1}$$

The SPARK Code

- Is a computational CFD code for hypersonic flows, maintained at IPFN.
- Is capable of handling Euler and Navier-Stokes formulations.
- Allows for the choice of a perfect, frozen or chemically reacting gas.
- Allows for the inclusion of chemical kinetic and thermal non-equilibrium models.

Mesh and Boundary Conditions

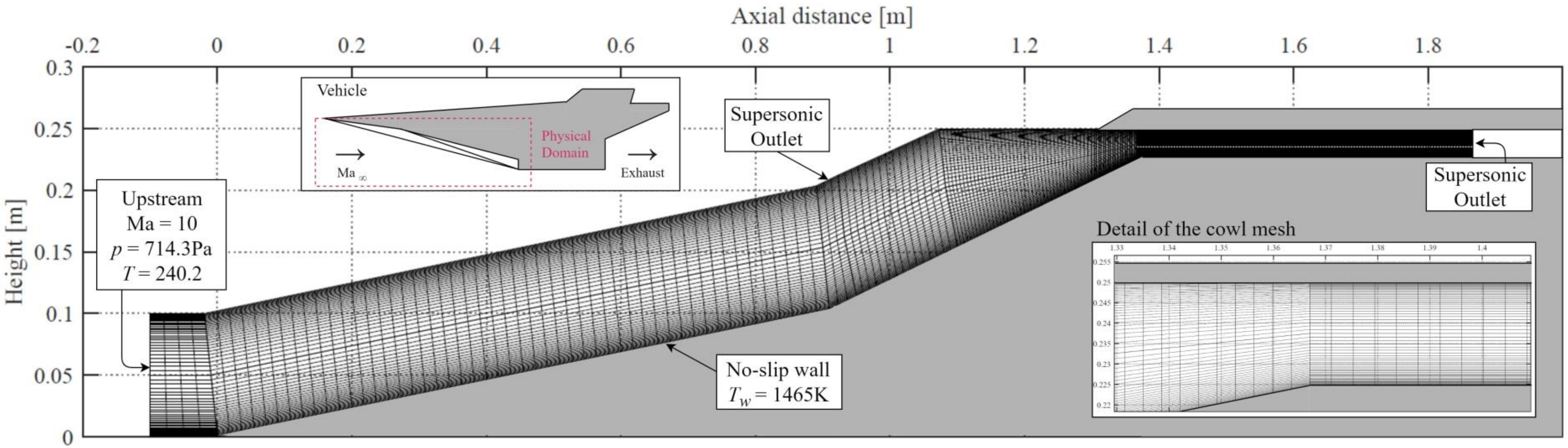

Fig. 7: Two-dimensional compression system mesh and boundary conditions. Not to scale.

Contents

Mesh Convergence Study

Four different grid configurations were compared at two locations to allow for the choice of an appropriate mesh.

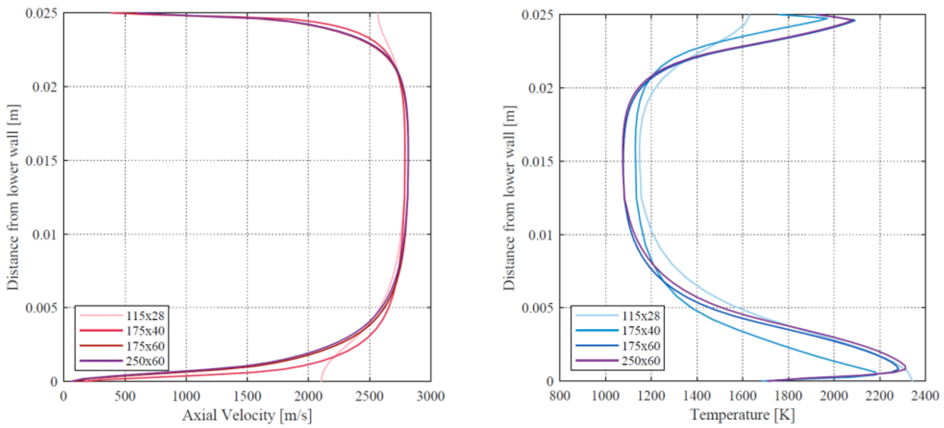

Fig. 8: Pressure and temperature profiles at x=1.1m, obtained for the mesh convergence study (2D).

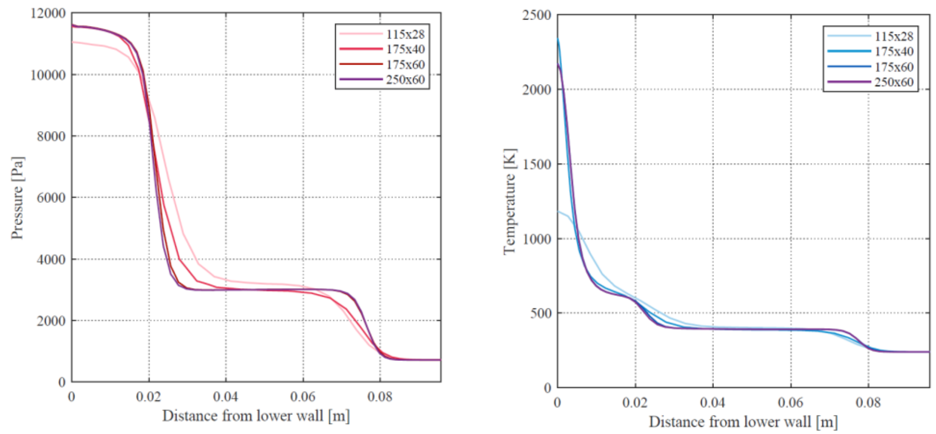

Fig. 9: Velocity and temperature profiles at the isolator exit, obtained for the mesh convergence study (2D).

The intermediate **175x60** grid was found to be the most suitable.

A similar mesh convergence study was conducted for the axisymmetric configuration and yielded an appropriate grid with **230x60** elements.

Two-Dimensional Geometry: Frozen Flow

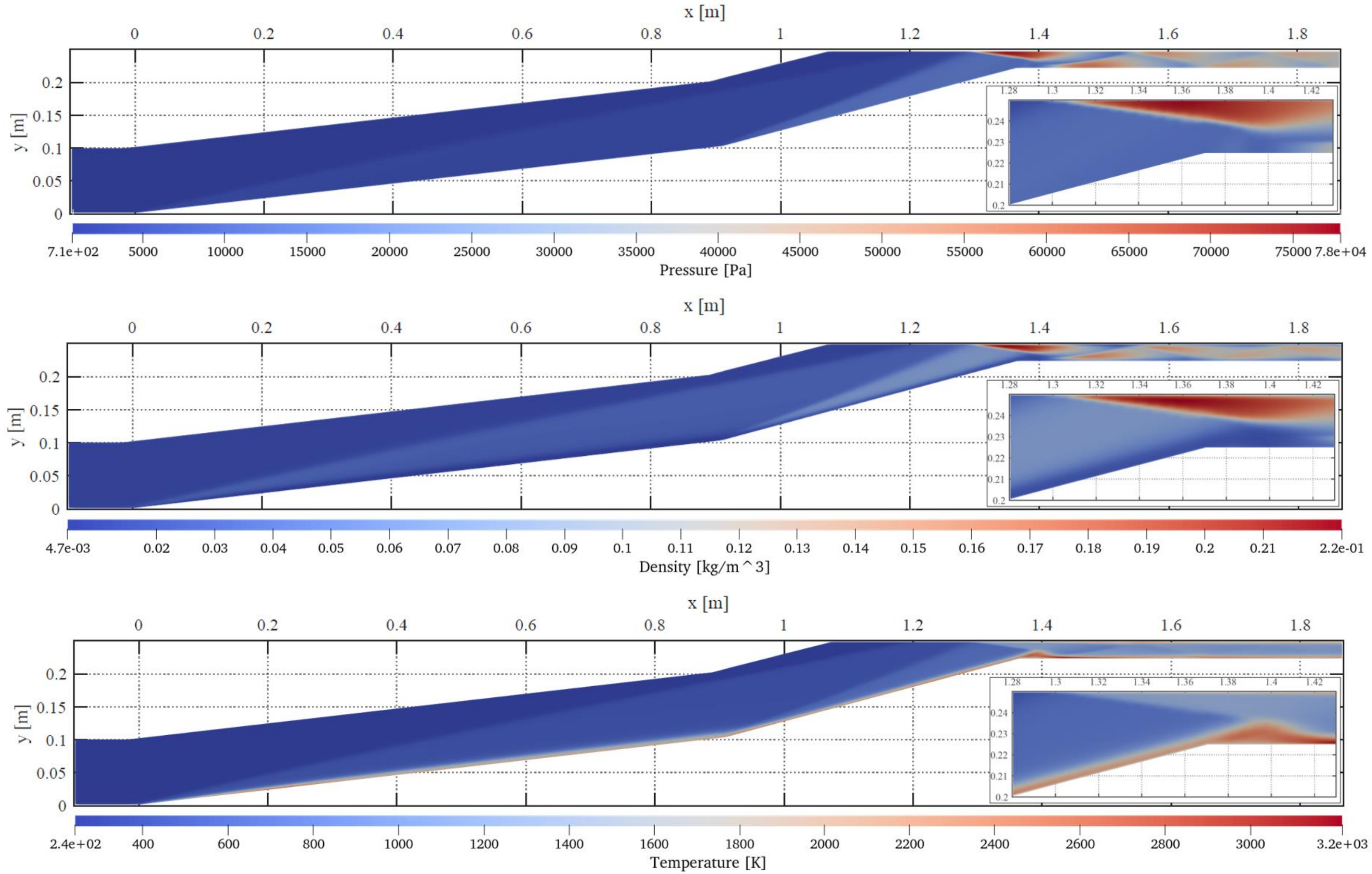

Fig. 10: Pressure, temperature and density fields obtained for the frozen-flow solution (2D).

Two-Dimensional Geometry: Frozen Flow

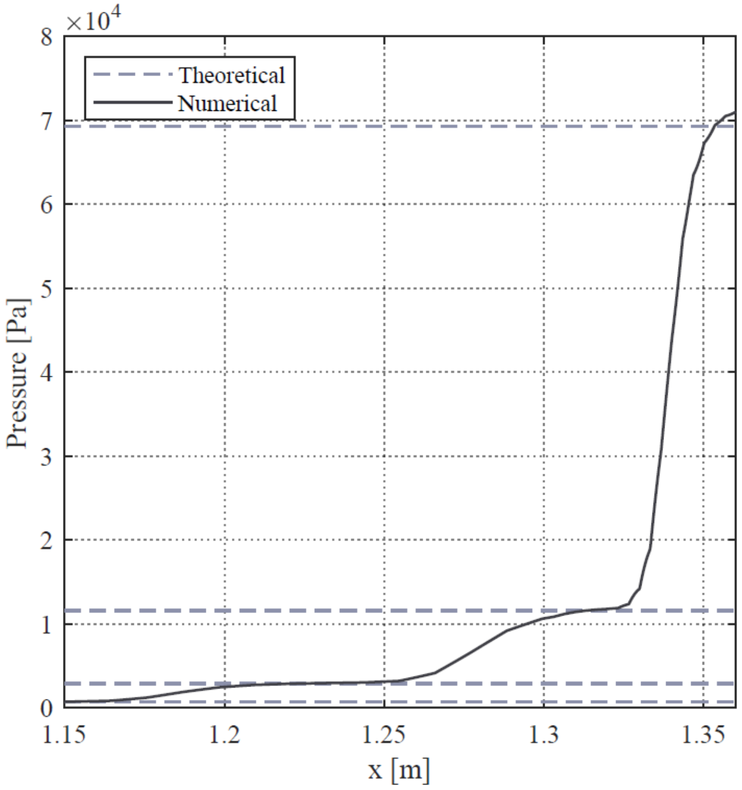

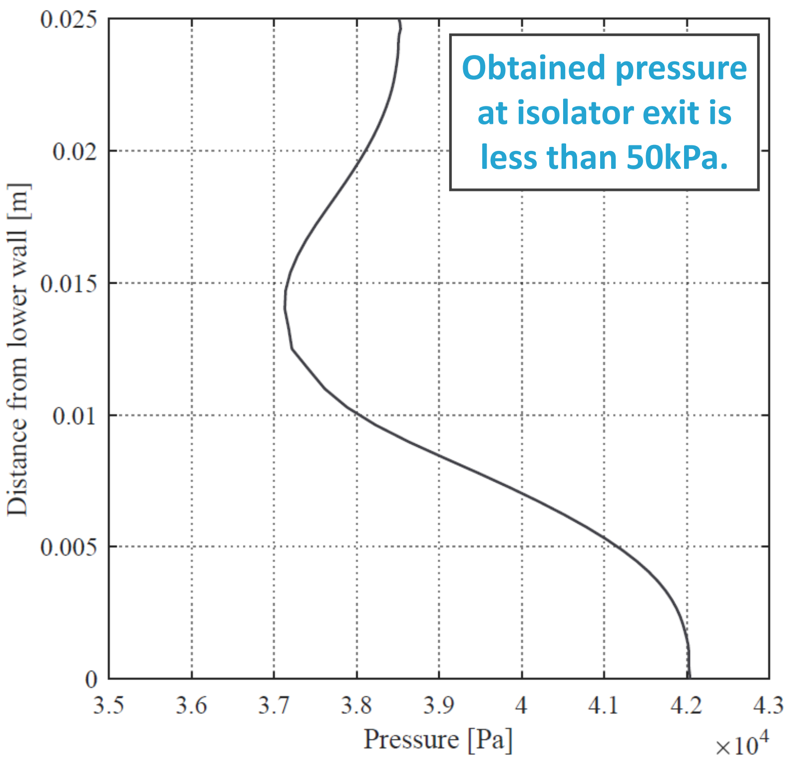

Fig. 11: Pressure variations across the first two oblique shock waves compared against oblique shock wave theory (left) and pressure profile at isolator exit (right).

Case	π_c	η_{KE}	η_c	$\dot{m}_c/\dot{m}_\infty$
Baseline	0.0793	0.9442	0.7898	0.7921

Table 2: Performance parameters for the baseline frozen flow solution.

Contents

Two-Dimensional Geometry: Impact of Wall Temperature

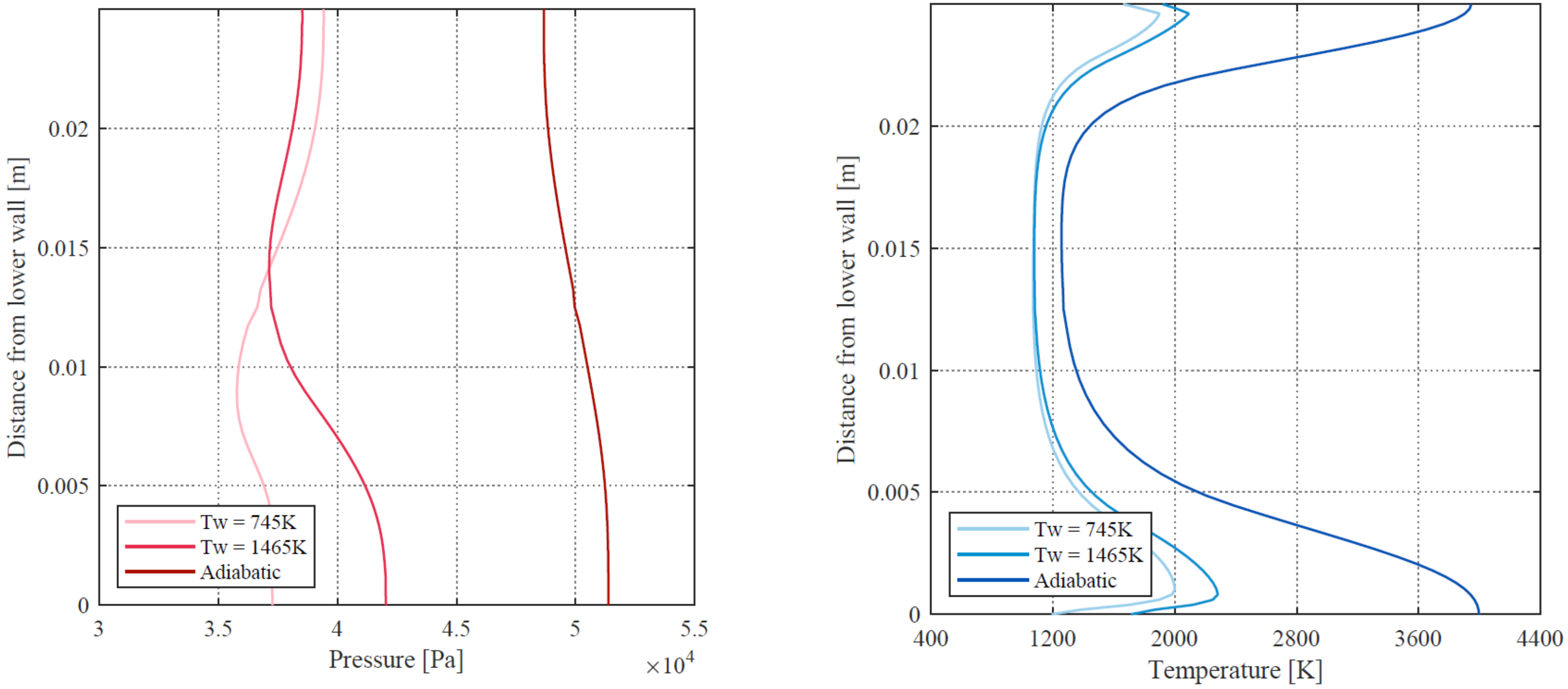

Fig. 12: Pressure and temperature profiles at the isolator exit for different wall boundary conditions.

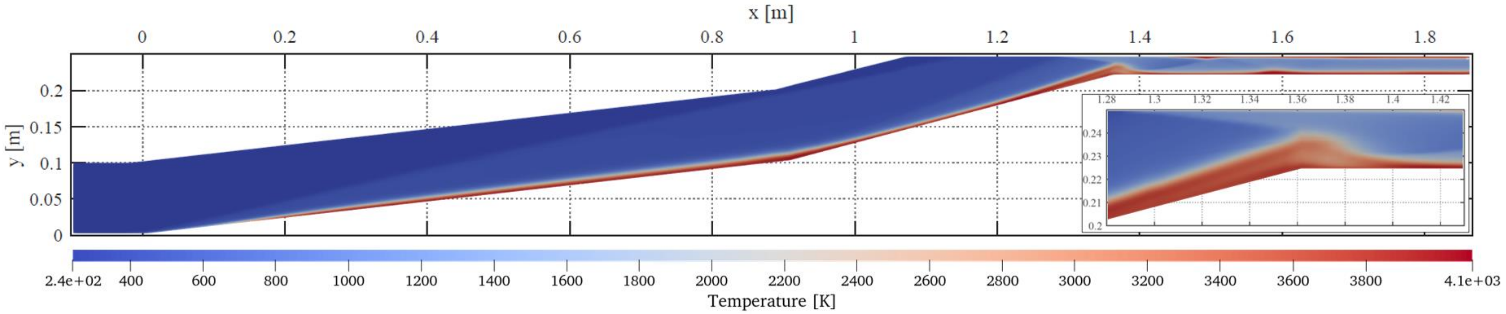

Fig. 13: Temperature field obtained for the adiabatic wall condition.

Contents

Two-Dimensional Geometry: Impact of Wall Temperature

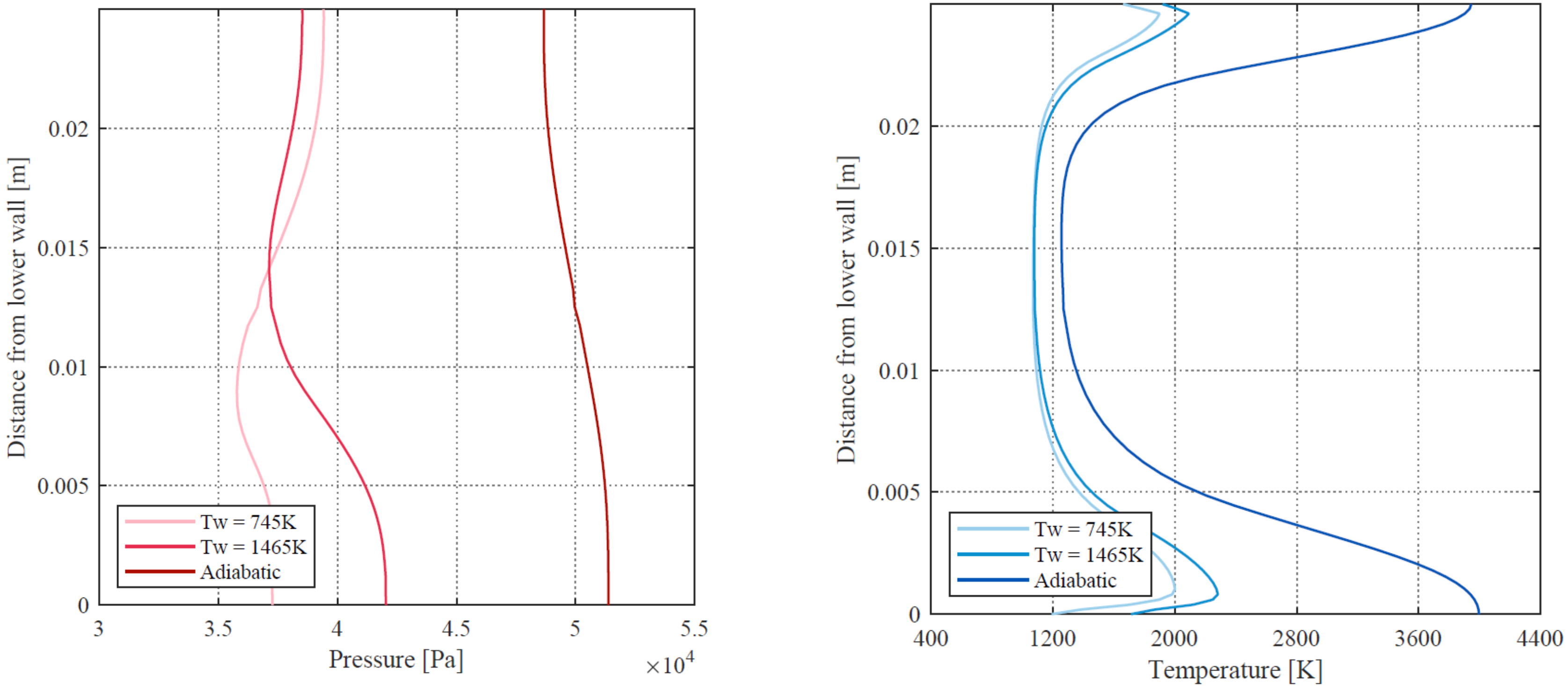

Fig. 12: Pressure and temperature profiles at the isolator exit for different wall boundary conditions.

Case	π_c	η_{KE}	η_c	$\dot{m}_c/\dot{m}_\infty$
T_w = 1465K	0.0793	0.9442	0.7898	0.7921
T_w = 745K	0.0908	0.9495	0.7956	0.8127
Adiabatic	0.0332	0.9035	0.7661	0.6925

Table 3: Performance parameters for different wall boundary conditions.

Contents

Two-Dimensional Geometry: Chemical and Thermal Non-Equilibrium

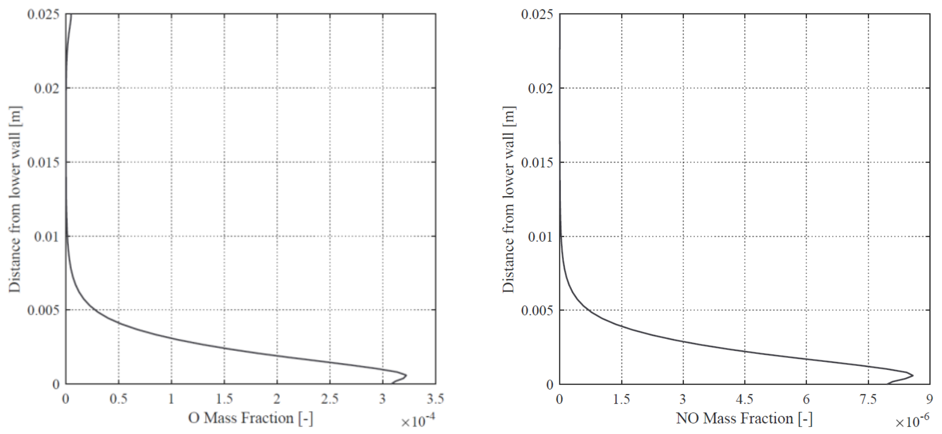

Fig. 14: O and NO mass fractions at the isolator exit for the chemically reacting flow solution.

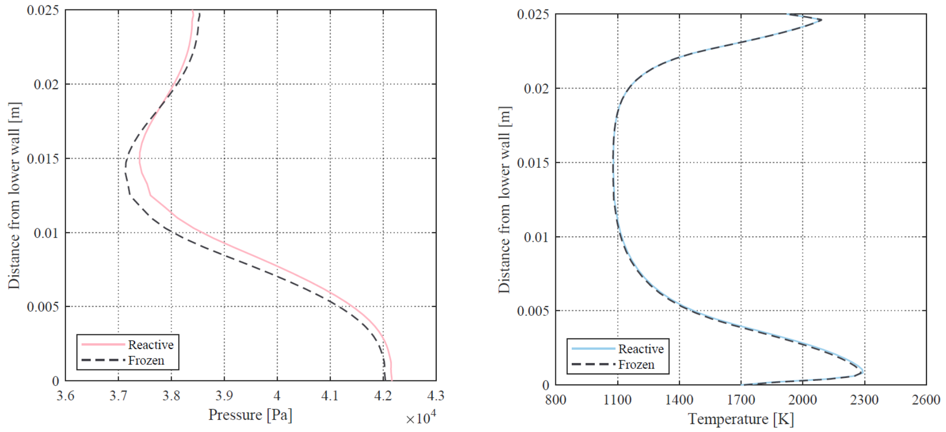

Fig. 15: Pressure and temperature profiles at the isolator exit for the chemically reacting flow solution.

Two-Dimensional Geometry: Chemical and Thermal Non-Equilibrium

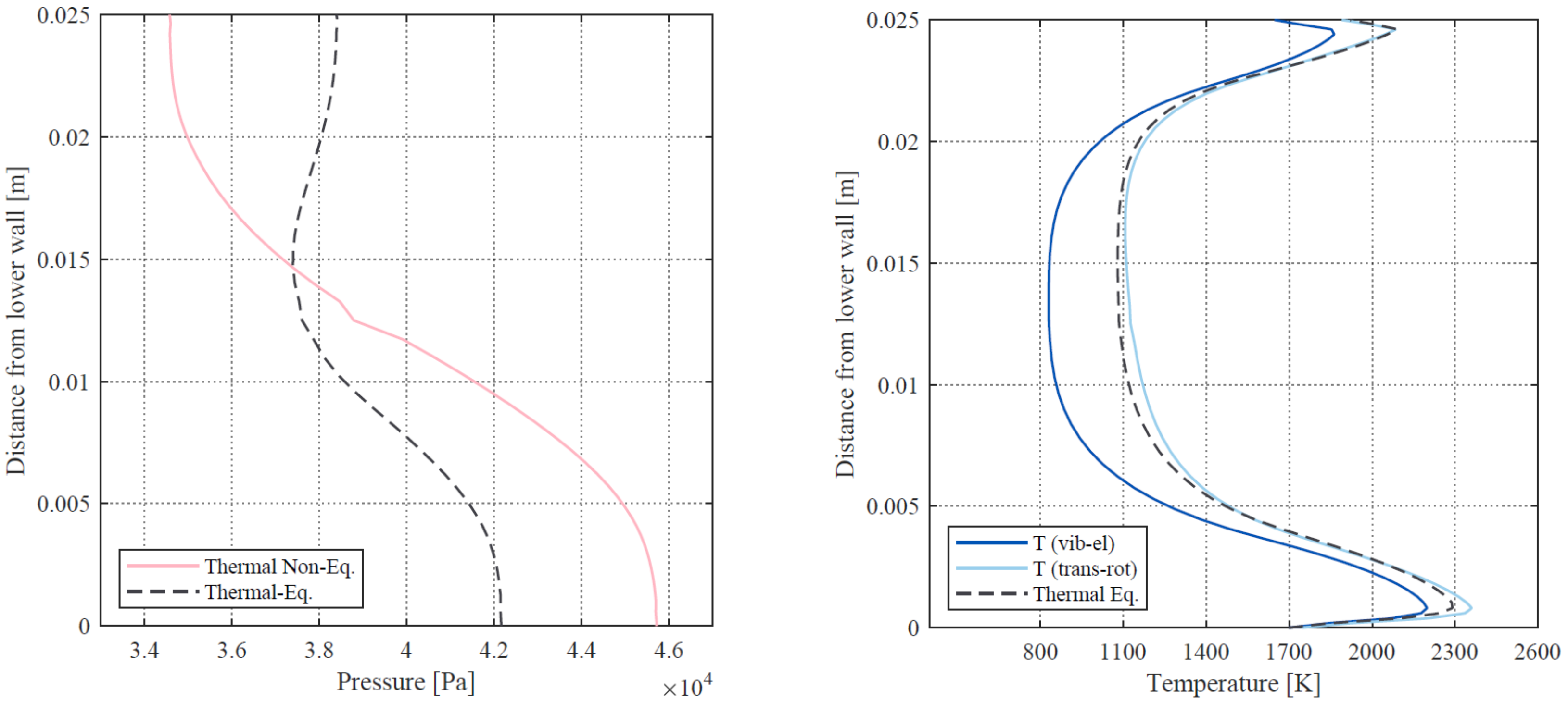

Fig. 16: Pressure and temperature profiles at the isolator exit for the thermal non-equilibrium flow solution.

Case		π_c	η_{KE}	η_c	$\dot{m}_c/\dot{m}_\infty$
Thermal Equilibrium	Frozen	0.0793	0.9442	0.7898	0.7921
	Reactive	0.0781	0.9440	0.7897	0.7916
Thermal Non-equilibrium		0.0652	0.9596	0.8183	0.7858

Expectedely, similar exit profiles lead to similar performance parameters.

Table 4: Performance parameters for thermal equilibrium and non-equilibrium solutions.

Axisymmetric Flow

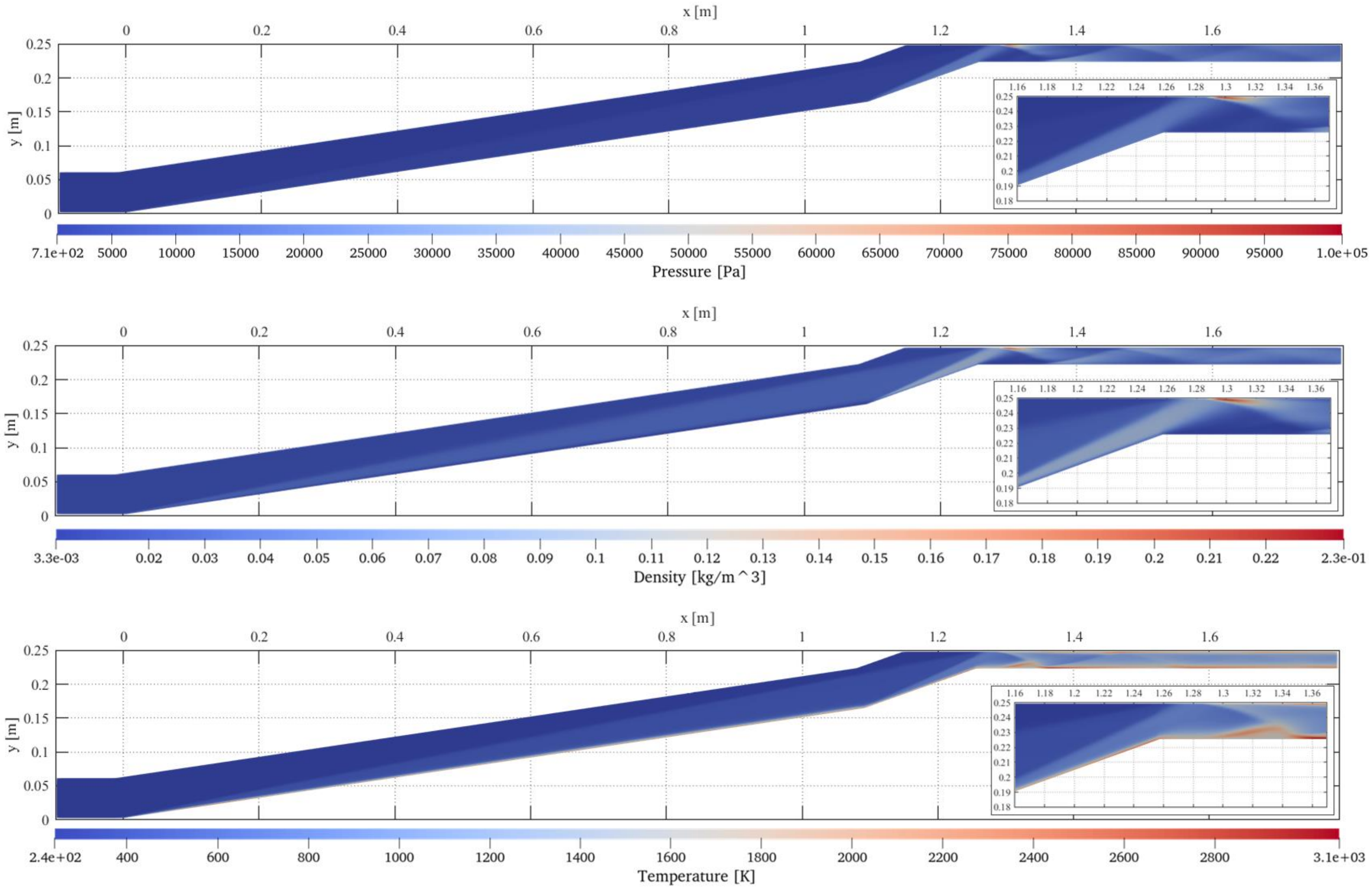

Fig. 17: Pressure, temperature and density fields obtained for the frozen-flow solution of the two-dimensional geometry.

Contents

Axisymmetric Flow

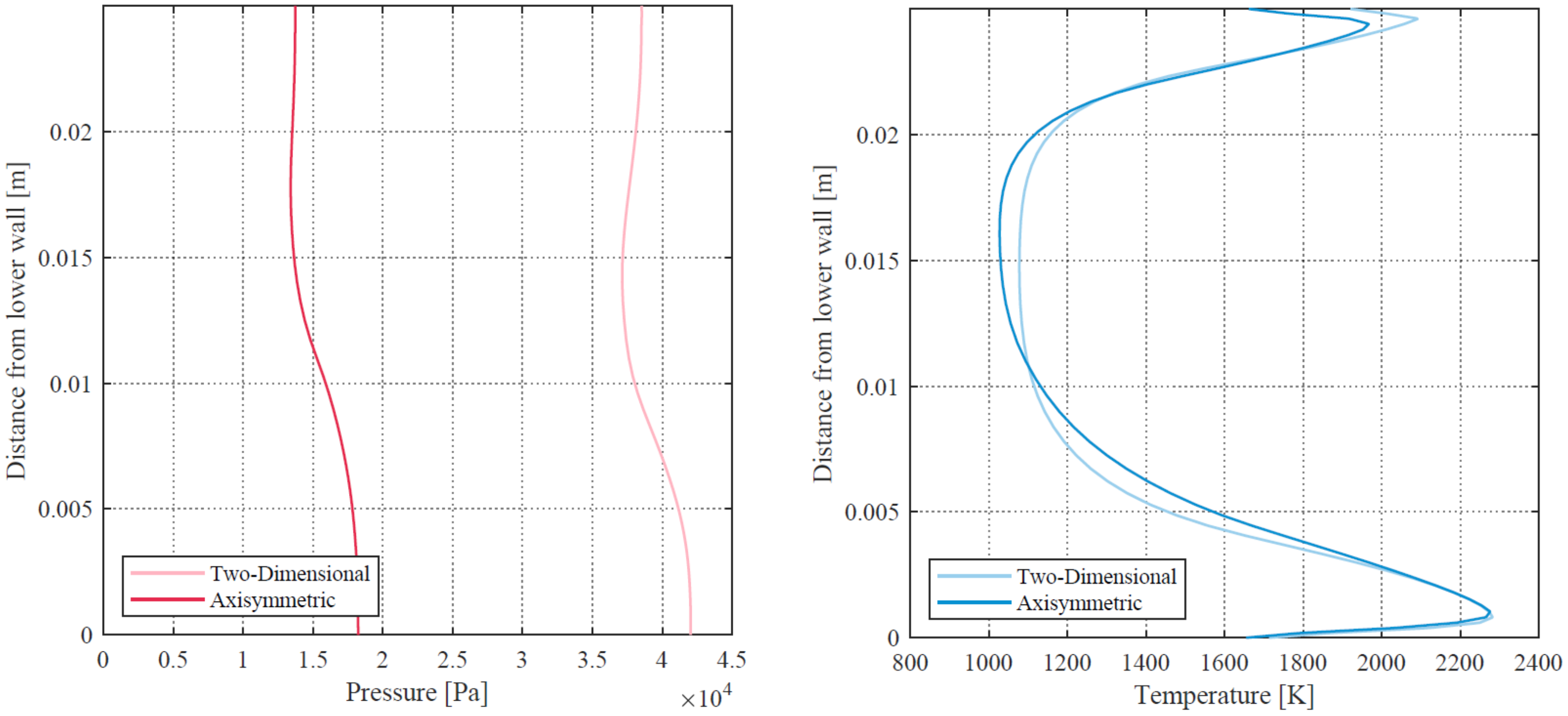

Fig. 18: Pressure and temperature profiles at the isolator exit, for the axissymetric and two-dimensional configurations.

Case		π_c	η_{KE}	η_c	$\dot{m}_c/\dot{m}_\infty$
Thermal Equilibrium	Frozen	0.0327	0.9181	0.6833	0.6276
	Reactive	0.0305	0.9172	0.6803	0.6068
Thermal Non-equilibrium		0.0243	0.9492	0.7274	0.5906

Table 5: Performance parameters for thermal equilibrium and non-equilibrium solutions.

Axisymmetric Flow

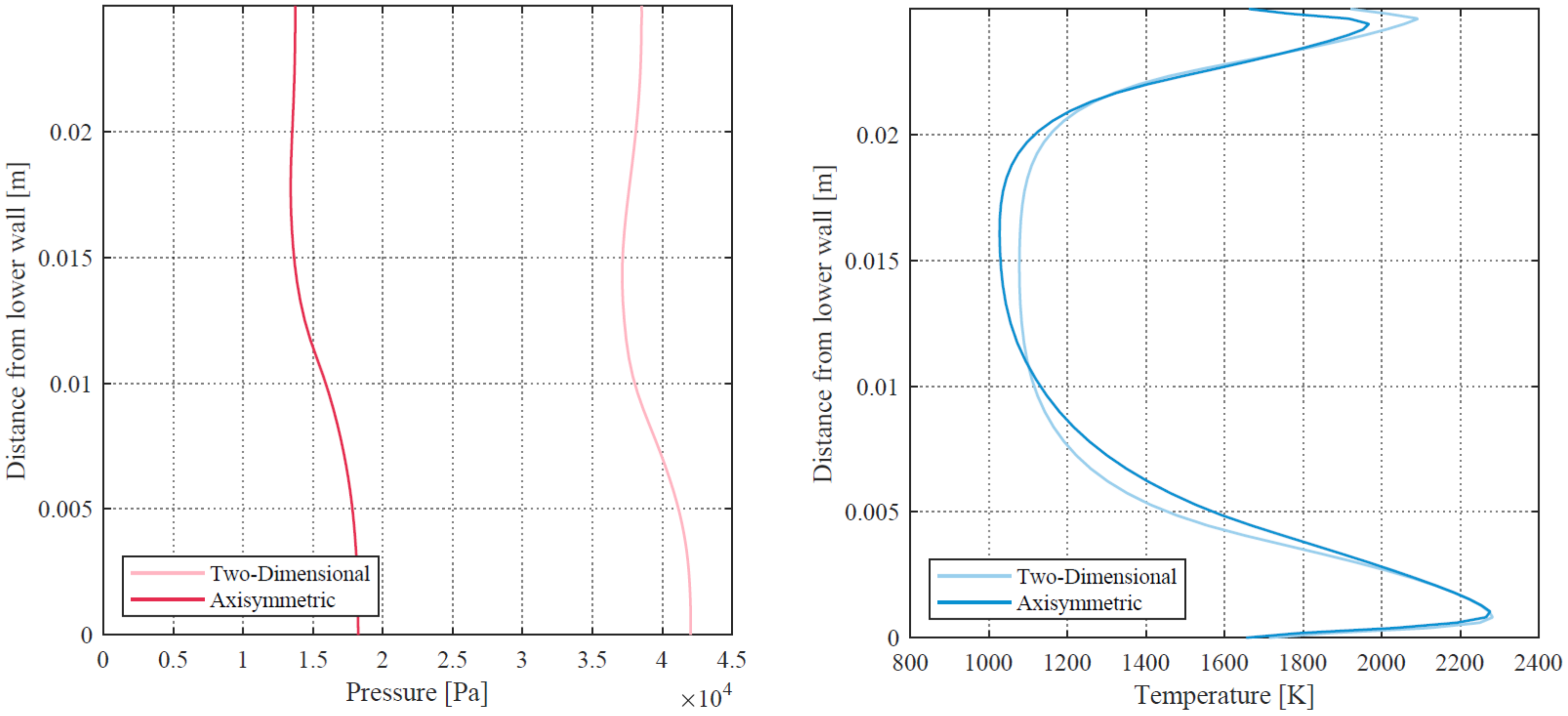

Fig. 19: Pressure and temperature profiles at the isolator exit, for the axissymetric and two-dimensional configurations.

Case		π_c	η_{KE}	η_c	$\dot{m}_c/\dot{m}_\infty$
Thermal Equilibrium	Frozen	0.0327	0.9181	0.6833	0.6276
	Reactive	0.0305	0.9172	0.6803	0.6068
Thermal Non-equilibrium		0.0243	0.9492	0.7274	0.5906

Table 5: Performance parameters for thermal equilibrium and non-equilibrium solutions.

Geometry Parametric Study: Increased Number of Ramps (2D)

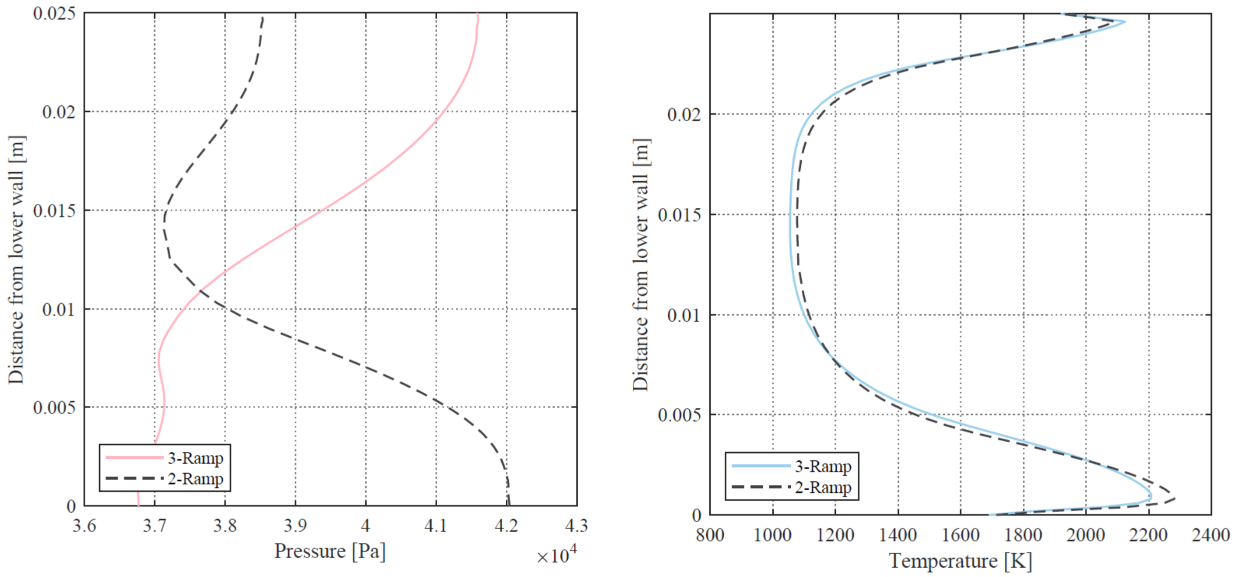

Fig. 20: Pressure and temperature profiles at the isolator exit, for different number of ramps.

Case	π_c	η_{KE}	η_c	$\dot{m}_c/\dot{m}_\infty$
Two Ramp	0.0793	0.9442	0.7898	0.7921
Three Ramp	0.0813	0.9449	0.7906	0.8061

Table 6: Performance parameters for different number of ramps.

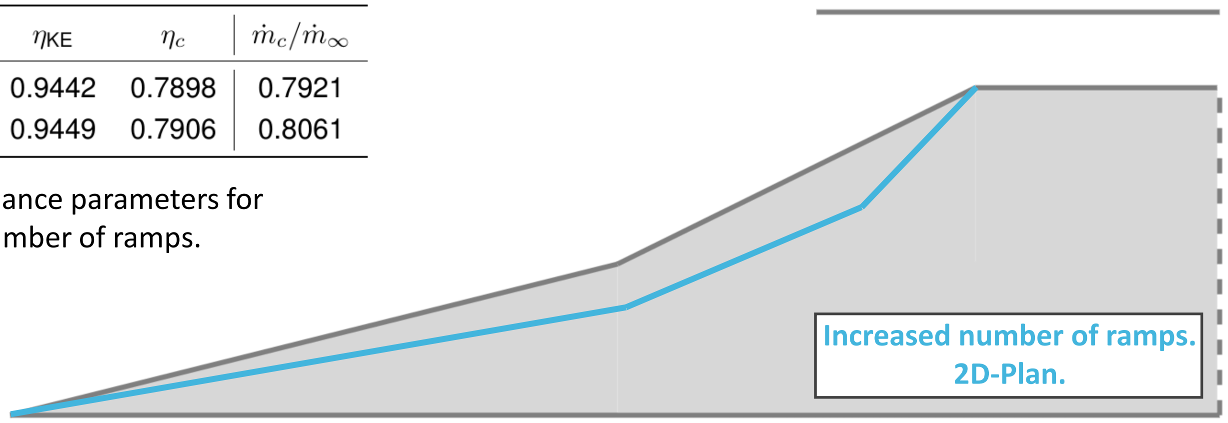

Contents

Geometry Parametric Study: Increased Compression Ratio (2D)

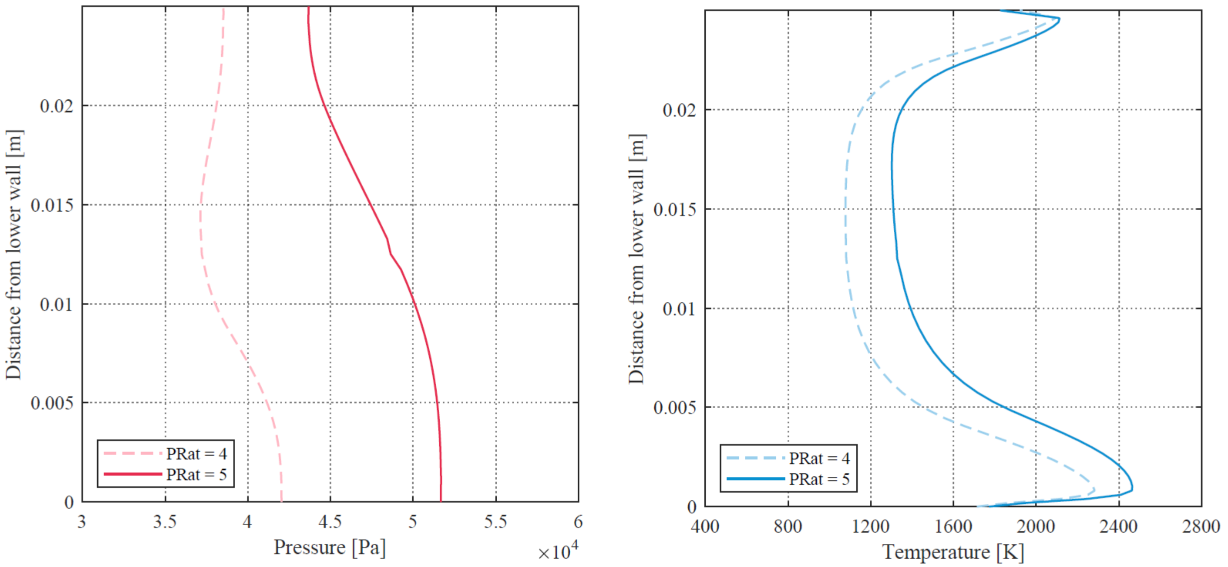

Fig. 21: Pressure and temperature profiles at the isolator exit, for different compression ratios.

Case	π_c	η_{KE}	η_c	$\dot{m}_c/\dot{m}_\infty$
PRat = 4	0.0793	0.9442	0.7898	0.7921
PRat = 5	0.0489	0.9317	0.7878	0.7859

Table 7: Performance parameters for different compression ratios.

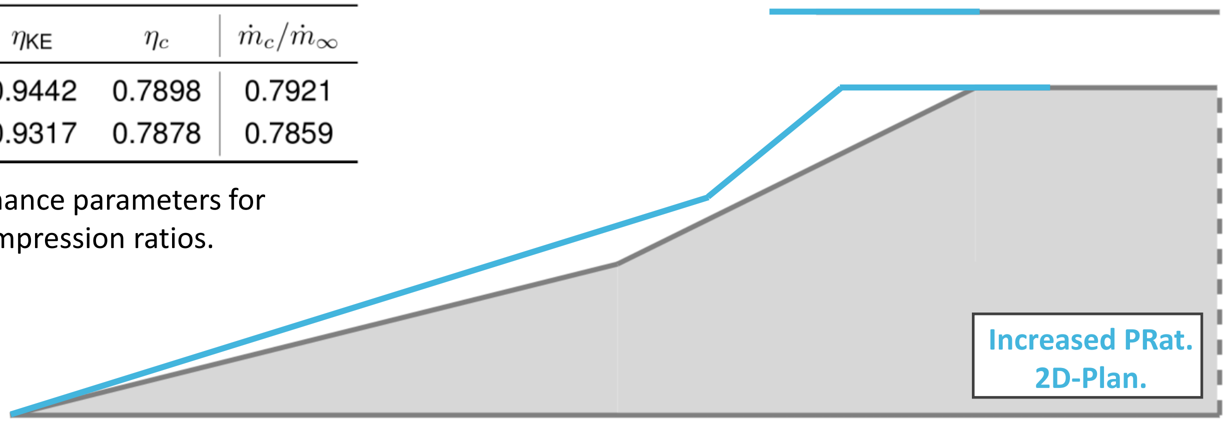

Geometry Parametric Study: Increased Compression Ratio (2D)

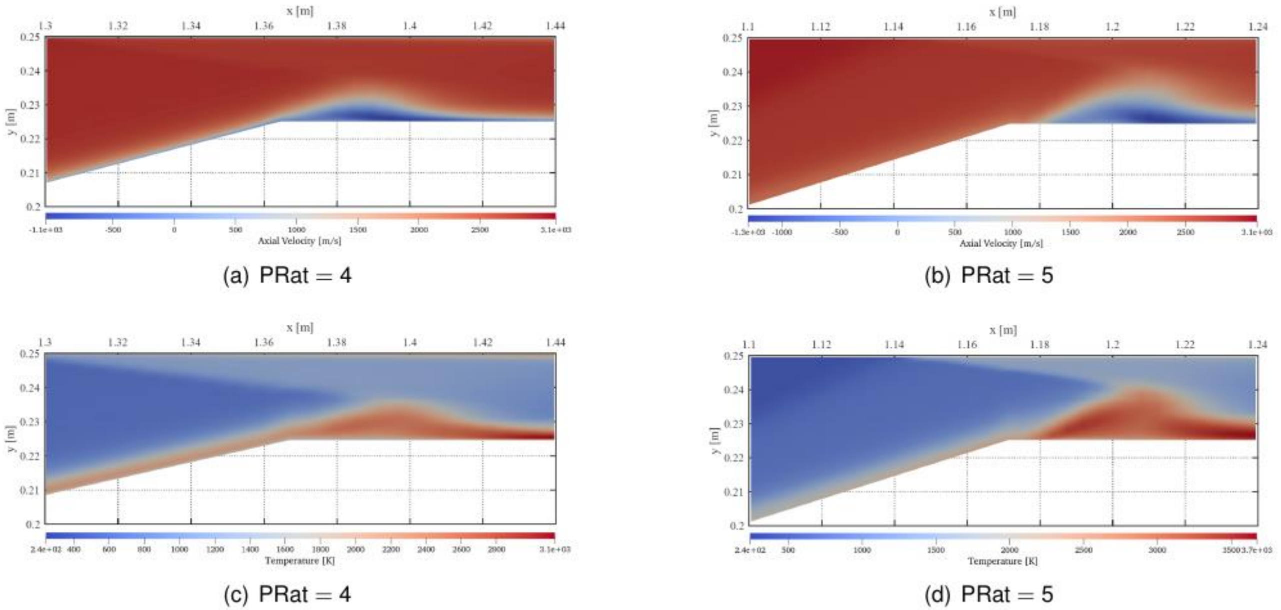

(a) PRat = 4 (b) PRat = 5

(c) PRat = 4 (d) PRat = 5

Fig. 22: Velocity (top) and temperature (bottom) profiles for different compression ratios.

Case	π_c	η_{KE}	η_c	$\dot{m}_c/\dot{m}_\infty$
PRat = 4	0.0793	0.9442	0.7898	0.7921
PRat = 5	0.0489	0.9317	0.7878	0.7859

Table 7: Performance parameters for different compression ratios.

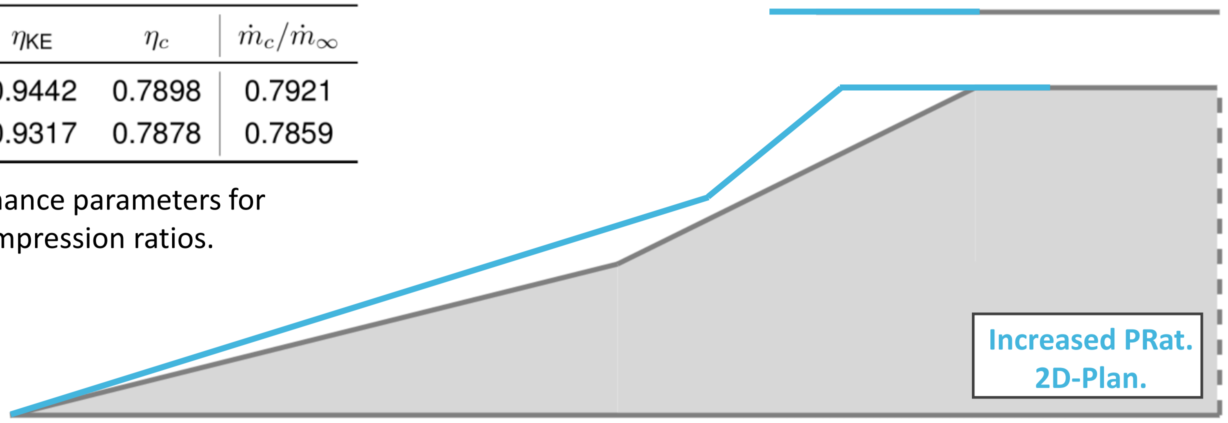

Contents

Geometry Parametric Study: Variation of the Isolator Length (2D)

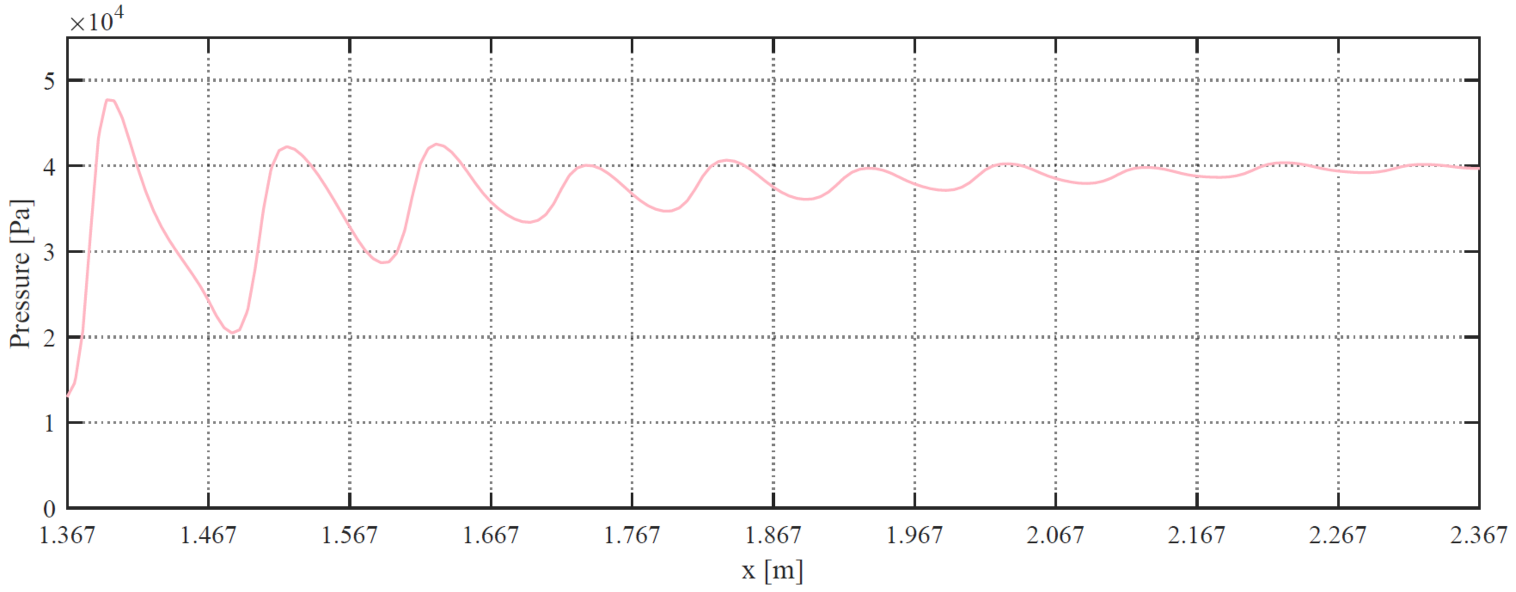

Fig. 23: Pressure along the isolator centreline, for an isolator length of 1m.

Case	π_c	η_{KE}	η_c	$\dot{m}_c/\dot{m}_\infty$
L = 0.15m	0.0983	0.9464	0.7919	0.8136
L = 0.5m	0.0793	0.9442	0.7898	0.7921
L = 1m	0.0697	0.9439	0.7915	0.7909

Table 8: Performance parameters for different compression ratios.

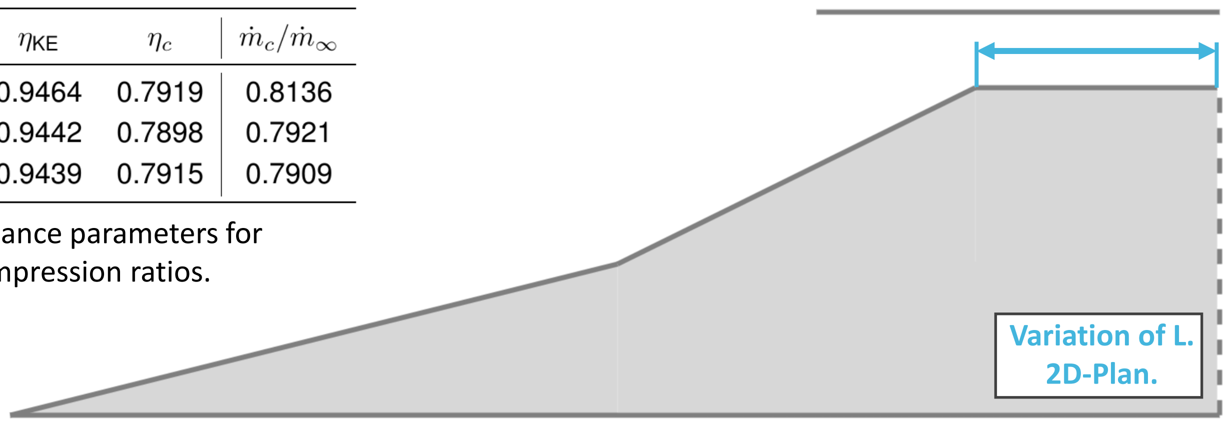

Geometry Parametric Study: Variation of the Isolator Length (2D)

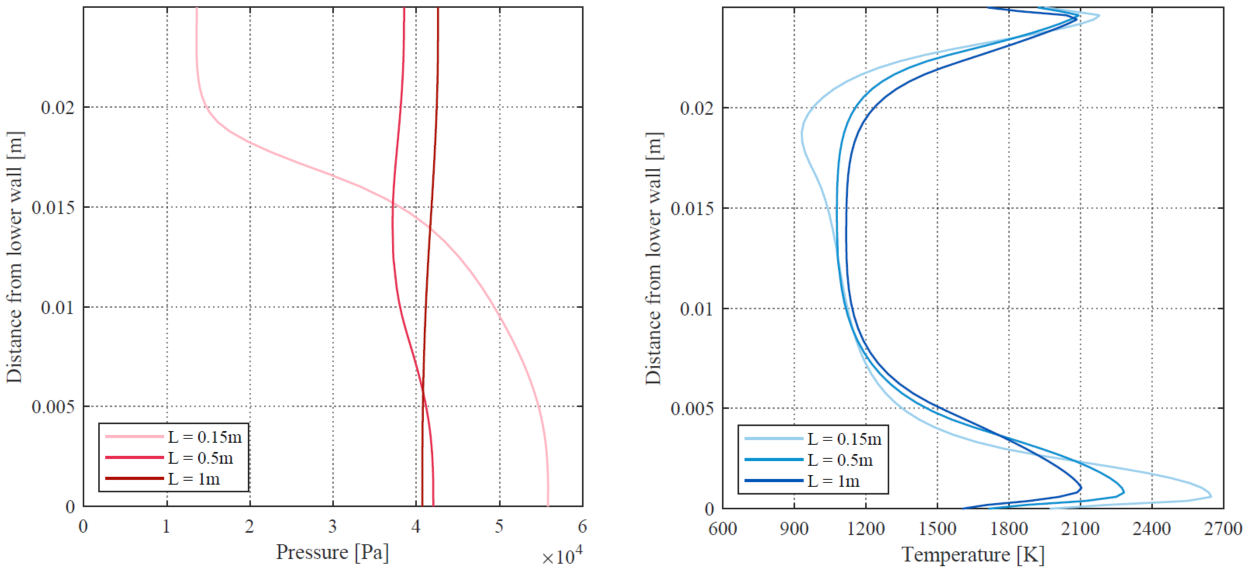

Fig. 24: Pressure and temperature profiles at the isolator exit, for different isolator lengths.

Case	π_c	η_{KE}	η_c	$\dot{m}_c/\dot{m}_\infty$
L = 0.15m	0.0983	0.9464	0.7919	0.8136
L = 0.5m	0.0793	0.9442	0.7898	0.7921
L = 1m	0.0697	0.9439	0.7915	0.7909

Table 8: Performance parameters for different compression ratios.

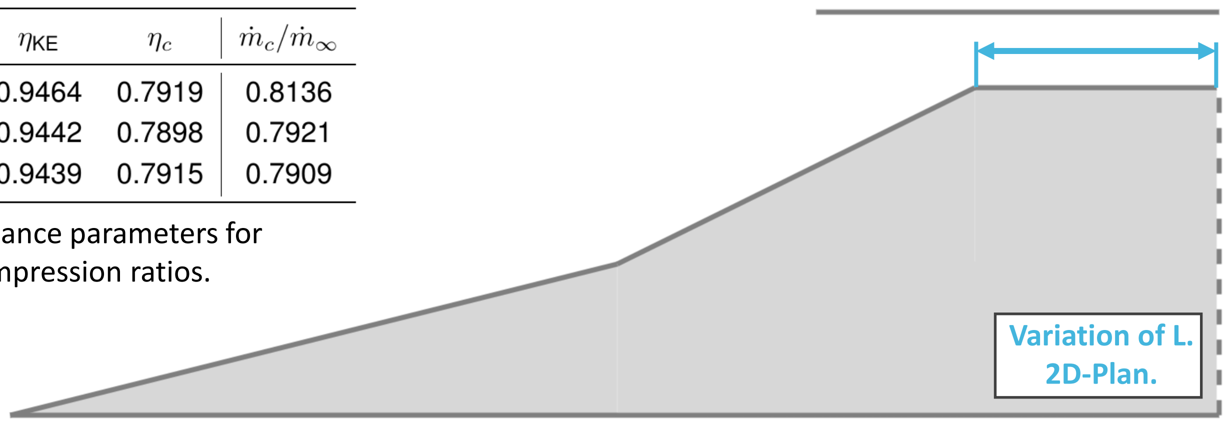

Contents

Geometry Parametric Study: Increased Contraction Ratio (2D)

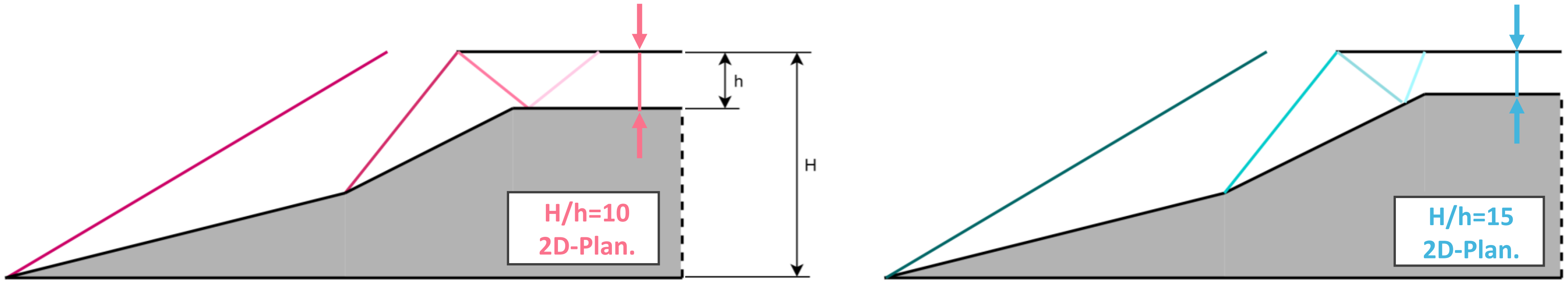

Fig. 25: Shock wave structure for a contraction ratio of 10 (left) and 15 (right).

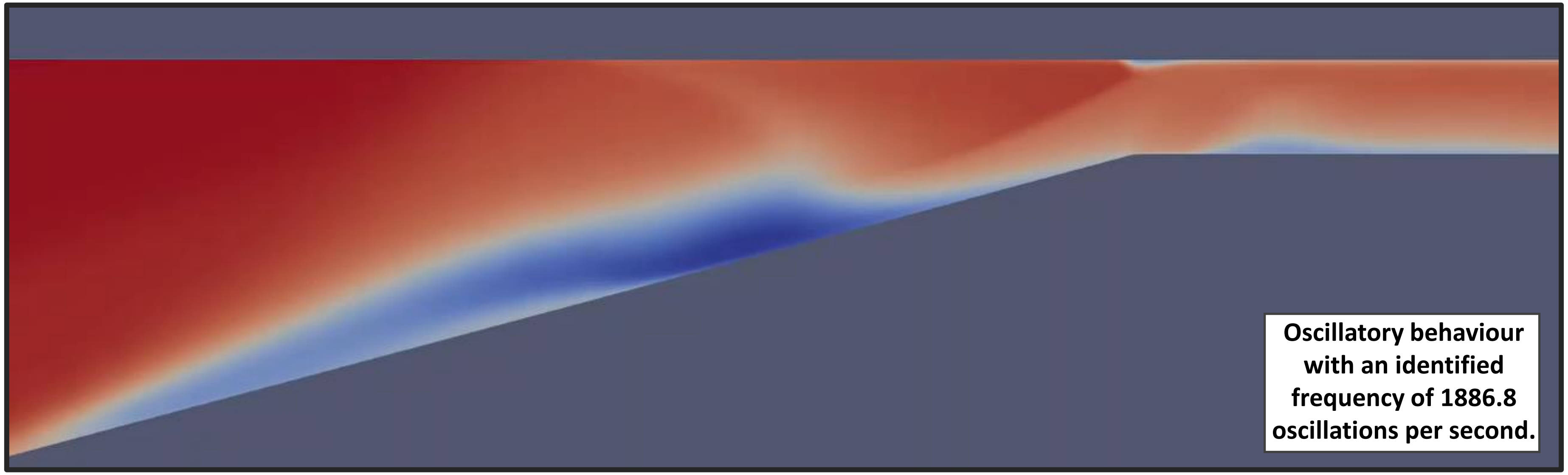

Fig. 26: Observed instabilitiy for the case with a contraction ratio of 15.

Contents

Geometry Parametric Study: Variation of the Expansion Corner Shape (2D)

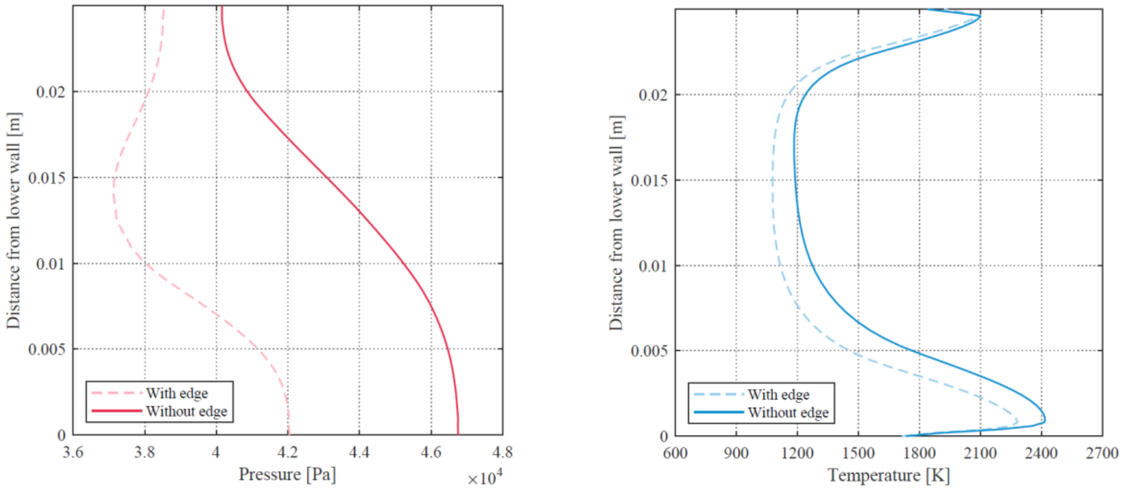

Fig. 27: Pressure and temperature profiles at the isolator exit, for different expansion corner shapes.

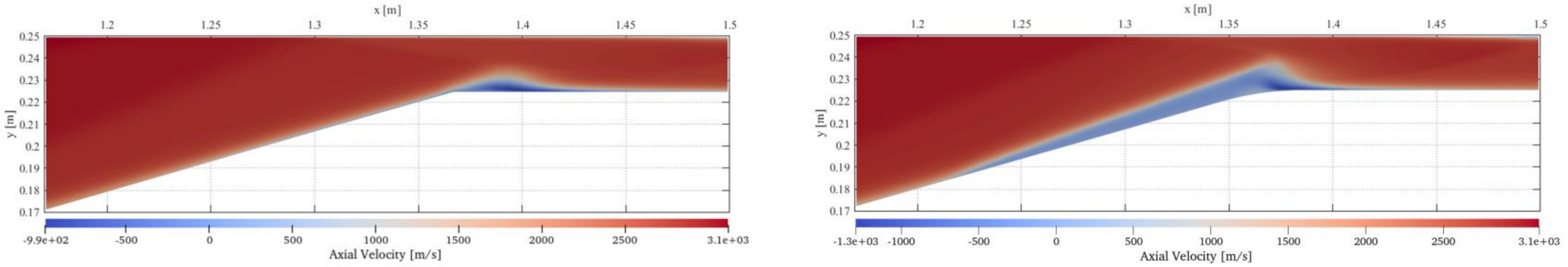

Fig. 28: Separation bubble for different expansion corner shapes.

Case	π_c	η_{KE}	η_c	$\dot{m}_c/\dot{m}_\infty$
With edge	0.0793	0.9442	0.7898	0.7921
Without edge	0.0598	0.9362	0.7869	0.7838

Table 9: Performance parameters for different expansion corner shapes.

Contents

Geometry Parametric Study: Axisymmetric Configuration

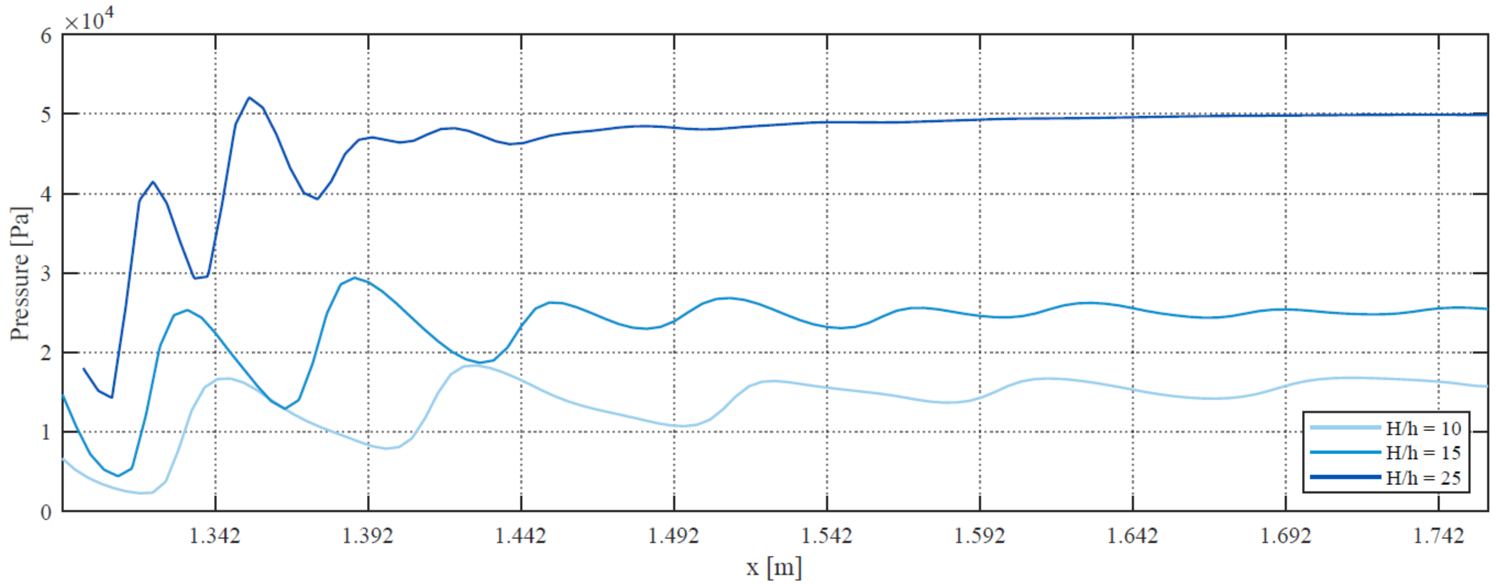

Fig. 29: Pressure along the isolator centreline, for different contraction ratios.

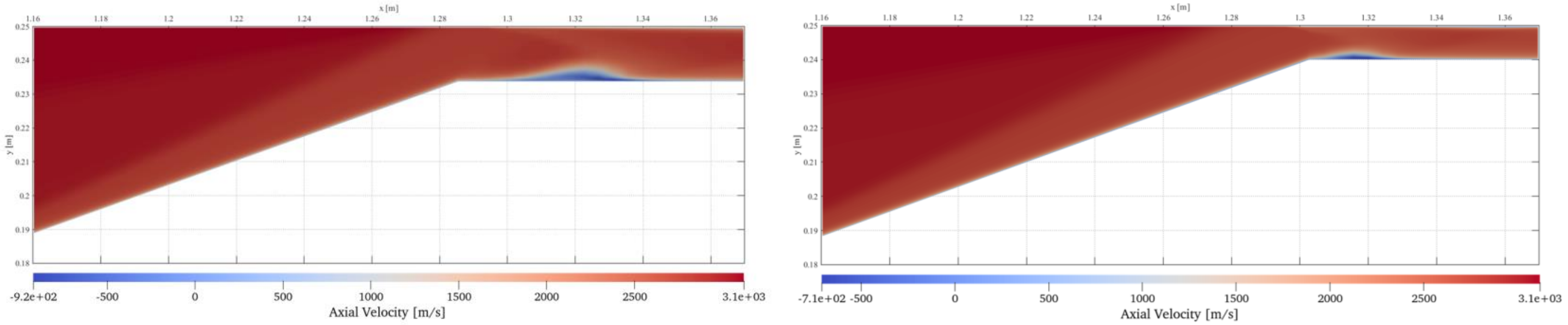

Figure 30: Separation bubbles for different contraction ratios.

Contents

Geometry Parametric Study: Axisymmetric Configuration

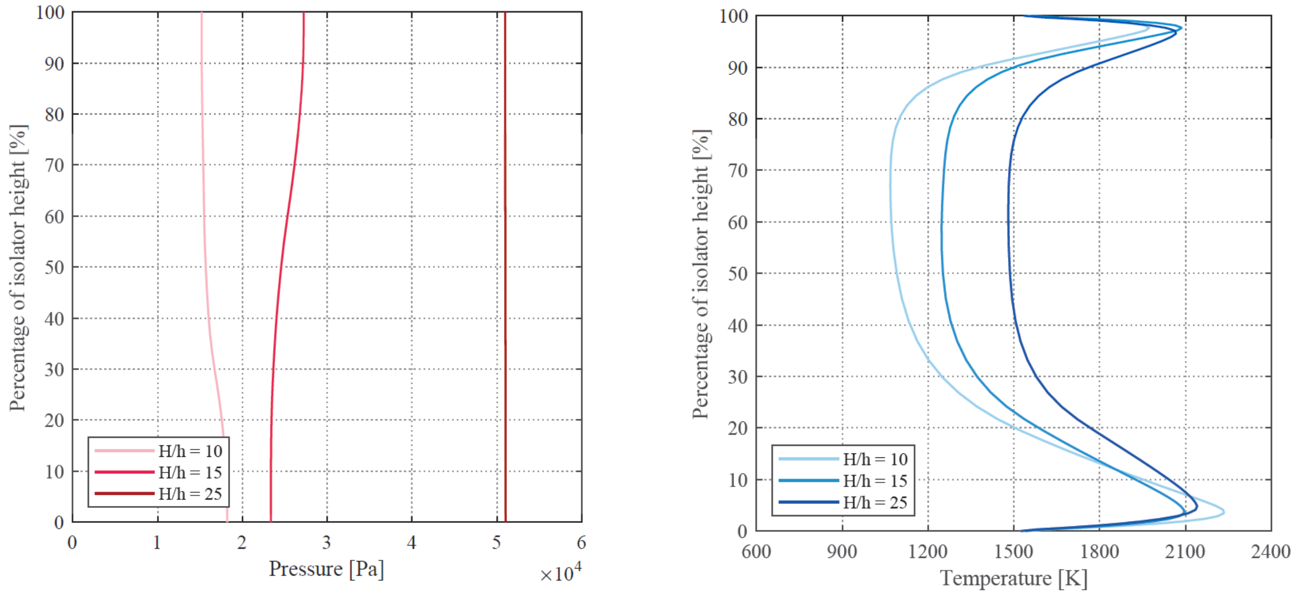

Fig. 31: Pressure along the isolator centreline, for different contraction ratios.

Case	π_c	η_{KE}	η_c	$\dot{m}_c/\dot{m}_\infty$
H/h = 10	0.0327	0.9181	0.6833	0.6276
H/h = 15	0.0350	0.9226	0.7285	0.5885
H/h = 25	0.0382	0.9314	0.7913	0.5975

Table 10: Performance parameters for different contraction ratios.

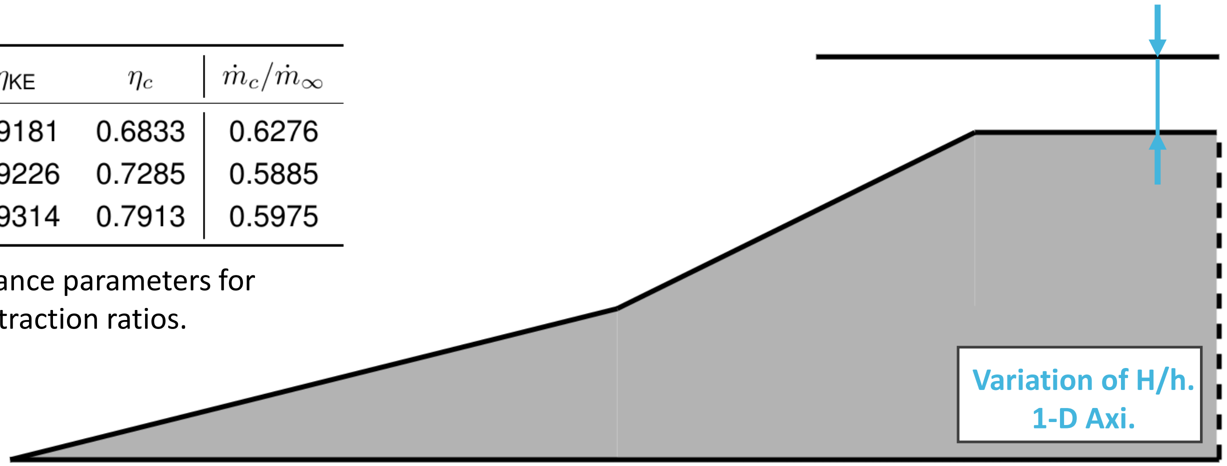

Contents

Off-Design Conditions: Mach 7

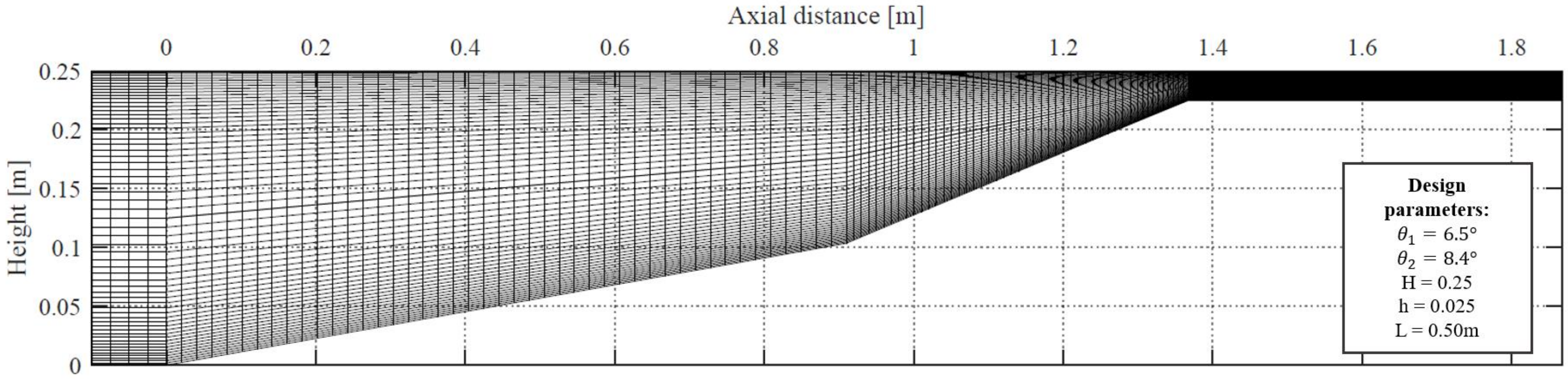

Fig. 32: Adapted grid used in the study of operation at off-design conditions.

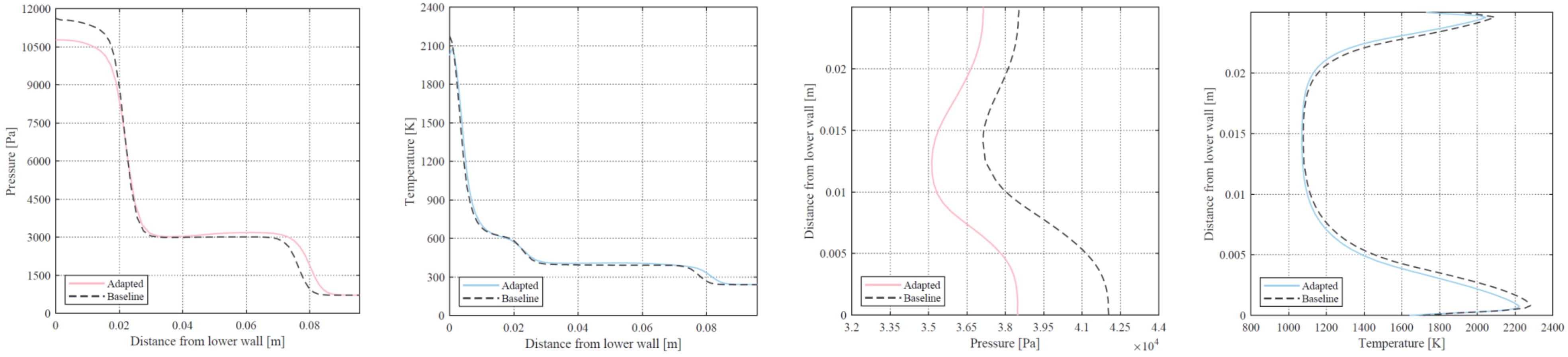

Fig. 33: Comparison of the baseline and adapted grids at a freestream Mach number of 10.

Contents

Off-Design Conditions: Mach 7

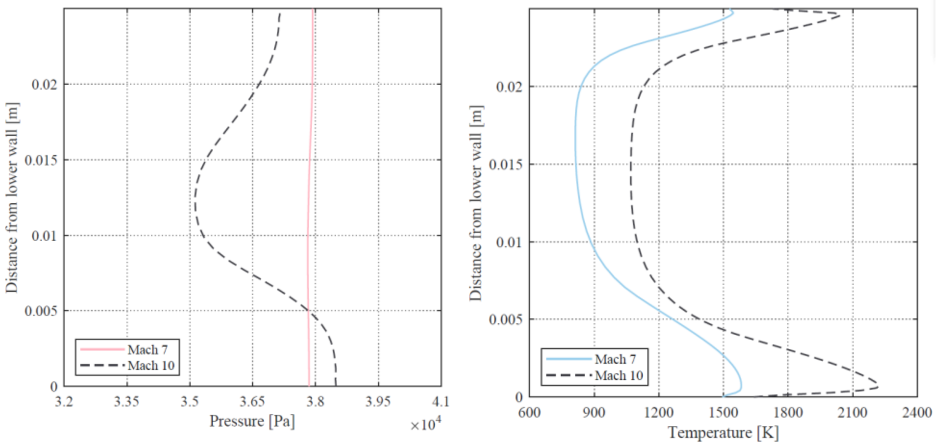

Fig. 34: Pressure and temperature profiles at the isolator exit, for different trajectory points (2D).

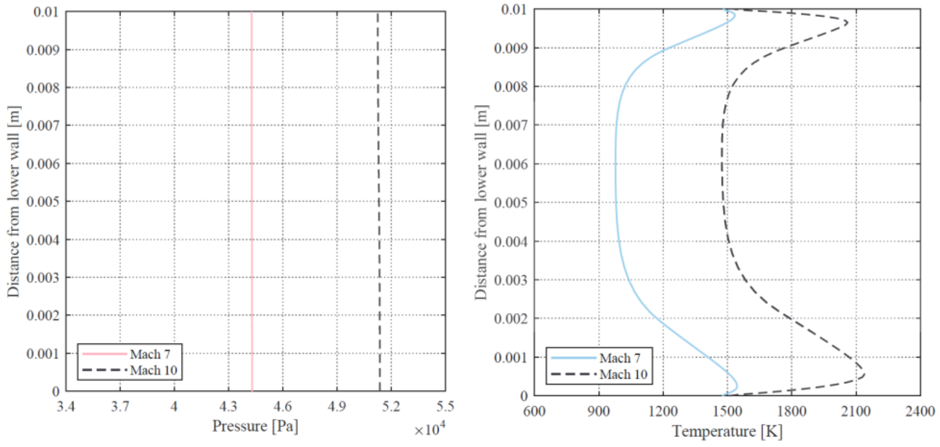

Fig. 35: Pressure and temperature profiles at the isolator exit , for different trajectory points (axysimmetric).

Case	π_c	η_{KE}	η_c	$\dot{m}_c/\dot{m}_\infty$
Mach 10	0.0833	0.9458	0.7880	0.7718
Mach 7	0.0896	0.8920	0.7370	0.4381

Table 11: Performance parameters for different trajectory points (2D).

Case	π_c	η_{KE}	η_c	$\dot{m}_c/\dot{m}_\infty$
Mach 10	0.0358	0.9316	0.7920	0.5922
Mach 7	0.0884	0.8914	0.7350	0.3355

Table 12: Performance parameters for different trajectory points (axisymmetric).

Contents

Achievements and Recommendations for Future Work

- Reproduction of a case study from the literature for a trajectory point of Mach 10, with **minor discrepancies found** in terms of peak pressure and isolator exit pressure;
- Lower wall temperatures were shown to improve performance, while an adiabatic wall results in unrealistically high wall temperatures.
- Chemical dissociation was found to be negligible while thermal non-equilibrium was found to occur and impact performance.
- An axisymmetric configuration was compared against a two-dimensional one, and was found to under-perform for all considered cases;
- The variation of some geometric parameters were shown to impact performance, with one geometric change leading to inlet unstart;
- Both the two-dimensional and axisymmetric configurations were **able to operate at an off-design trajectory point** of Mach 7.

Fig. 36: Burrows Kurkov [7] frozen flow simulation already implemented in SPARK.

Fig. 37: Attempt to reproduce the supersonic combustions experiments conducted in the DLR facilities in SPARK.

Contents

Achievements and Recommendations for Future Work

- Reproduction of a case study from the literature for a trajectory point of Mach 10, with **minor discrepancies found** in terms of peak pressure and isolator exit pressure;
- Lower wall temperatures were shown to improve performance, while an adiabatic wall results in unrealistically high temperatures.
- Chemical dissociation was found to be negligible while thermal non-equilibrium was found to occur and impact performance.
- An axisymmetric configuration was compared against a two-dimensional one and was found to under-perform for all considered cases;
- The variation of some geometric parameters were shown to impact performance, with one geometric change leading to inlet unstart;
- Both the two-dimensional and axisymmetric configurations were **able to operate at an off-design trajectory point** of Mach 7.

Fig. 36: Burrows Kurkov **[7]** frozen flow simulation already implemented in SPARK.

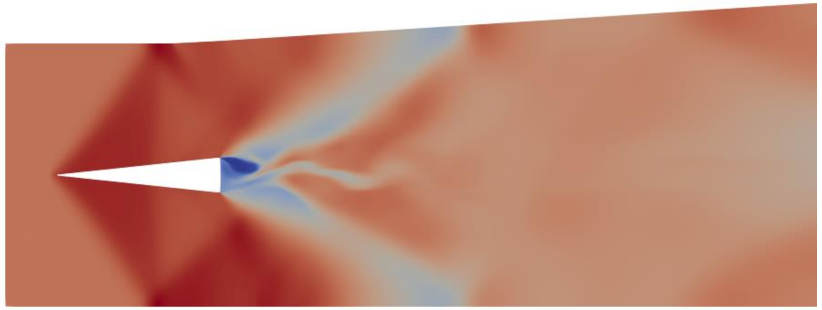

Fig. 37: Attempt to reproduce the supersonic combustions experiments conducted in the DLR facilities **[8]** in SPARK.

Contents

Bibliography

[1] Scramjet concept art. Retrieved January 18th, 2021 at https://www.scienceabc.com/innovation/what-is-a-scramjet-engine.html.

[2] The compression, combustion, and expansion regions of turbojet, ramjet, and scramjet engines. Retrieved October 8th, 2020, at https://en.wikipedia.org/wiki/Scramjet.

[3] W. H. Heiser and D. T. Pratt. Hypersonic Airbreathing Propulsion. AIAA Education Series, 1994. ISBN:978-1563470356.

[4] D. Andreadis. Scramjet engines enabling the seamless integration of air and space operations. Pratt and Whitney, 2004.

[5] L. H. Quan, N. P. Hung, L. D. Quang, and V. N. Long. Analysis and design of a scramjet engine inlet operating from Mach 5 to Mach 10. International Journal of Mechanical Engineering and Applications, 4(1):11–23, Feb. 2016. doi: 10.11648/j.ijmea.20160401.12.

[6] A. Tahsini. Combustion efficiency and pressure loss balance for the supersonic combustor. Proceedings of the Institution of Mechanical Engineers, Part G: Journal of Aerospace Engineering, 234(6):1149–1156, 2019. doi: 10.1177/0954410019895885.

[7] Burrows and Kurkov Supersonic Mixing: Frozen Chemistry, consulted at: https://www.grc.nasa.gov/WWW/wind/valid /bk/study01/bk1.html.

[8] Oevermann, M.. Aerospace science and Technology. Numerical investigation of turbulent hydrogen combustion in a SCRAMJET using flamelet modeling, 4(7):463–480, 2000. https://doi.org/10.1016/S1270-9638(00)01070-1.

ipfn
INSTITUTO DE PLASMAS E FUSÃO NUCLEAR